Delft University of Technology

Master Thesis
Chemical engineering

The Feasibility of Proton Boron Capture Therapy

A computational study

by

Tuur Vermunt

to obtain the degree Master of Science
at the Delft University of Technology,
to be defended publicly January 31st, 2019 at 11:00 am.

Student number:	4178084	
Project duration:	09-04-2018 - 31-01-2019	
Thesis committee:	dr. Z. Perkó	TU Delft, supervisor
	prof. dr. H.Th. Wolterbeek	TU Delft, supervisor
	prof. dr. J.L. Kloosterman	TU Delft, chair
	dr. D. Lathouwers	TU Delft
	dr. A.G. Denkova	TU Delft

TU Delft

Abstract

Proton therapy efficiency can be described as the ratio between tumour and non-tumour dose, while the tumour receives the planned dose. This efficiency is limited by the energy deposition property of the proton. To enhance the efficiency beyond this physical limit, targeted nuclear reactions during proton therapy could be exploited. For this purpose the ^{11}B(p,3α) reaction has been researched. The three alpha particles created have a high linear energy transfer (LET) and cause an increase in energy deposited at the reaction site. This reaction has a high cross section for low proton energies and protons have a low energy in the tumour area. Hence, proton ^{11}B capture will more frequently occur in the tumour area, which can increase the tumour to non-tumour dose.

Proton boron capture therapy (PBCT) has been studied, using Monte Carlo simulation and by conducting experiments, which suggested a 90 and 50% increase in energy deposited respectively. However, these results were contradicted by other research, stating the ^{11}B(p,3α) reaction could not significantly increase energy deposited during proton therapy. This discussion formed the foundation of this thesis.

Two Monte Carlo methods, MCNP6 and Geant4, were used to investigate the reproducibility of the results obtained in previous research. First, MCNP6 simulations were done, which did not result in significant dose increase for proton therapy. To investigate the reproducibility of MCNP6 a second Monte Carlo method, Geant4, was used. Geant4 simulations produced similar results to MCNP6, equally not reproducing the promising results of previous research.

Neither Monte Carlo method included all possible reaction cross sections for alpha particle creation during PBCT. Therefore, a simple Boltzmann model was made to simulate proton and alpha particle transport, including these missing reaction cross sections. To simulate the effect of below 1 MeV proton boron capture, a non-dynamic Boltzmann model was used, which resulted in a non significant increase in alpha production during PBCT. Afterwards, an alpha-proton-alpha avalanche reaction was investigated. For the effects of this reaction to be investigated a dynamic Boltzmann model was used, which resulted in no significant increase in alpha production either.

To investigate if the ^{11}B(p,3α) reaction could cause the increase in cell death found by experimental work, the cell killing potential of each alpha particle created was calculated analytically. Using the alpha production rate from the non-dynamic model, this calculation resulted in ten cells killed per alpha particle created. The alpha particles created during PBCT have a track length similar to the size of one cell, therefore it is unlikely for an alpha particle to kill ten cell.

None of the obtained results, provide evidence that the ^{11}B(p,3α) reaction will enhance the efficiency of proton therapy. Thus, we hypothesize that the experimental results could be related to boron having a radio sensitizing effect on cells. To test this irradiating boronated cells with gamma rays is proposed as the next step for further research.

Acknowledgements

I would like to express my gratitude towards the people who helped and inspired me during the course of this thesis. First, I would like to thank Zoltán, for supervising me for the last nine months. This supervision was especially valuable when I had the great idea I knew better what a flux was, than everybody else in the world. I also want to thank Bert for suggesting this project after finding this interesting topic debated heavily in literature and always taking time to discuss my research and coming up with new insights to determine the next steps.

Lastly, I want to thank my girlfriend Joia for her mental support. In particular her continued support during the final weeks before the deadline, as I have not been the most fun person to be around.

Contents

1 Introduction

1.1 Proton therapy

Currently, the 5-year survival rates for adults and children diagnosed with cancer are approximately 65% and 80% respectively [1]. Fifty percent of these cancer patients receive radiotherapy during their treatment trajectory [2], which is associated with high incidence rates of treatment related morbidity [3], including organ damage, secondary malignancies, and other late side effects. With cancer survival rates increasing, healthy tissue sparing treatment methods are becoming more important. One such method is proton therapy, which has been introduced by Wilson in 1946 as a new radiation option for treatment of tumours while reducing damage to healthy tissues [4].

A key advantage of proton therapy is the excellent spatial dose distribution in the patient. A proton beam has inherent tissue sparing capabilities and is therefore of interest for use in future tumour treatments [5, 6]. The importance of sparing non-tumorous tissues differs per tumour type and size, mainly depending on the near lying organs at risk (OAR). To spare healthy tissues proton therapy utilizes the Bragg peak characteristic of protons in matter [4]. Figure 1.1 shows a comparison of a photon versus a proton beam for irradiation of a deep-seated tumour.

The photon beam in Figure 1.1 is a basic photon beam, currently more advanced methods like intensity modulated radiation therapy (IMRT) or RapidArc (RA) are available. While these advanced photon therapy methods are as accurate as proton in ensuring the target receives the planned radiation dose [7], the unwanted dose is mostly redistributed. This redistribution is due to the physical properties of X-rays [8].

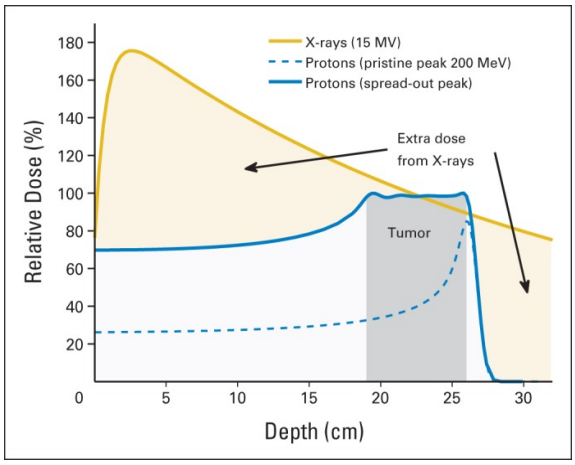

Figure 1.1: The comparison of relative dose delivered during tumour treatment for a proton beam (blue) and x-ray beam (yellow). The proton dose is made up tens of pristine Bragg peaks resulting in the spread out Bragg peak. Source: [9].

For proton, and other charged particle therapies, the Bragg peak is the reason for having an excellent spatial dose distribution. Charged particles show this dose delivery, compared to non-charged particles due to their interaction with electrons. The energy loss for moving particles is not constant but increases with decreasing energy which results in a pristine Bragg peak for dose delivered, shown as the blue dotted line in Figure 1.1.

1.2 Proton interaction with matter

Protons moving trough matter interact with this matter in different ways. These interactions can be with electrons, Coulomb scattering and nuclear interactions.

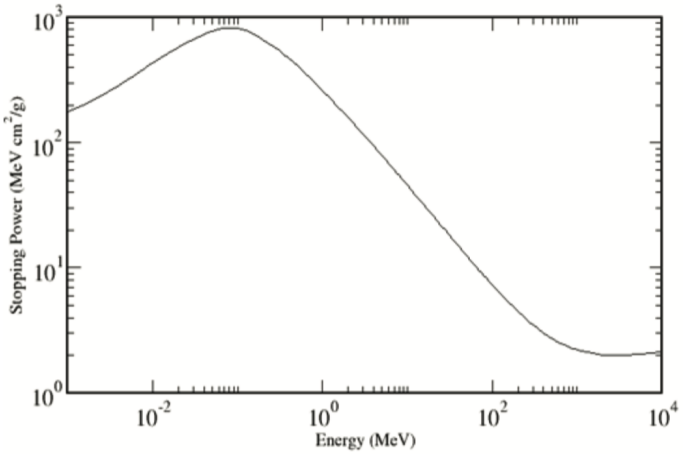

Figure 1.2: The stopping power of a proton in water for proton energies from 1 keV up to 1e4 MeV. The data for this figure is obtained from the NIST database [10].

1.2.1 Stopping power

The slowing down of protons in matter is described by the stopping power $S(E)$ (see Equation 1.1), which is the energy loss dE per unit path length dx traveled trough the medium. Figure 1.2 shows the stopping power increases with a decreasing energy. The stopping power is mainly caused by electromagnetic interactions, causing electrons to be exited, or ionization of target material to occur. In the therapeutic energy range, proton-electron interactions are the main cause of proton energy loss.

$$S(E) = -\frac{dE}{dx} \tag{1.1}$$

1.2.2 Scattering

When protons pass closely by the nucleus a minor deflection can occur, due to the Coulomb interaction with this nucleus. Even though for one interaction this deflection might be negligible, the combination of multiple Coulomb scattering events result in angular variation of protons in the beam. This angular variety causes the beam to widen as it transverses through matter, which is described to be near Gaussian [11].

1.2.3 Nuclear reactions

Proton nuclear reactions occur in the human body, when the proton energy is above 7 MeV. The main isotopes for proton nuclear reactions are ^{12}C and ^{16}O, which can create secondary particles like neutrons, prompt gammas, alpha particles or secondary protons. Secondary particles have a small contribution to the delivered dose during treatment as only 1% of the total proton energy is transferred to secondary particles [12]. Created neutrons and photons can escape the patient, however secondary protons and alpha particles still deliver the dose in the patient.

1.3 Boron capture therapy

For radiation therapy, efficiency can be described as the ratio between tumour and non-tumour dose, while the tumour receives the planned dose. This efficiency is limited by the physical properties of the source particle, since particles deposit dose as they travel to the tumour. Targeted nuclear reactions might be used to extend the efficiency beyond these physical limits.

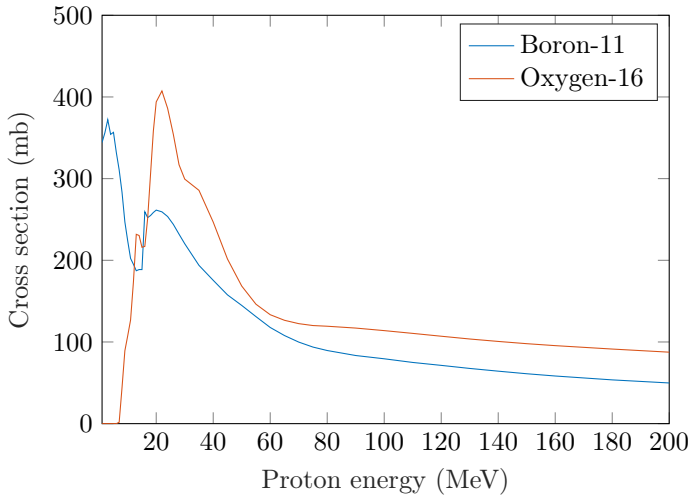

Figure 1.3: The cross section for proton capture versus energy, for ^{16}O and ^{11}B. At low energies (below 7 MeV) the ^{16}O cross section goes to zero, and the ^{11}B cross section peaks.

1.3.1 Boron neutron capture therapy (BNCT)

A typical example of targeted nuclear reaction therapy is boron neutron capture therapy, which uses thermal neutrons to induce a reaction (^{10}B(n,α)), instead of delivering the particles energy to the target. These neutrons are captured by ^{10}B, having a capture cross section of 3740 barn. Following the capture an alpha particle is released and the recoil atom is ^{7}Li:

$$n + {}^{10}B \rightarrow \alpha + {}^{7}Li\ (\ +\ 2.31MeV)[13].$$

The linear energy transfer (LET) of the alpha particles is high and almost all energy is deposited at the reaction site. Because the reaction occurs along the complete path of the neutron, controlling this reaction is mainly performed by using a boronated tumour-targeting agent [14]. BNCT was used to treat patients with photon therapy resistant and recurring head and neck tumours [15]. Although this was only palliative treatment, it was effective in increasing quality of life for these patients. However, to apply BNCT more widely, new boronated tumour targeting agents need to be developed, which have a higher tumour to non-tumour tissue uptake ratio [16].

1.3.2 Proton boron capture therapy (PBCT)

^{11}B could also be used to enhance the effectiveness of proton therapy. Proton boron capture therapy uses the reaction:

$$p + {}^{11}B \rightarrow 3\alpha\ (\ +\ 8.7MeV).$$

The three alpha particles cause an extra 8.7 MeV energy to be deposited at the reaction site. The alpha particles have a higher relative biological effectiveness than protons, therefore this energy deposition should be multiplied by a factor twenty to obtain effective delivered dose. The cross section of the reaction is shown in Figure 1.3, excluding the resonance cross section peak at 665 keV, which is documented as high as 2.7 barn [17]. The ^{11}B cross section increases with decreasing proton energy and gets higher than the ^{16}O cross section for protons below 30 Mev. The average proton energy continuously decreases, when approaching the tumour. Thus, protons below 30 MeV should mainly exist in the tumour region, as the Bragg peak is aimed to be inside the tumour. This decreasing average proton energy combined with a pristine Bragg peak is shown in Figure 1.4.

The proton ^{11}B reaction can deliver an extra dose, while no targeting of the boron will be needed, due to cross section having a peak for low energy protons, which are only present in the tumour area. Therefore, the proton boron capture reaction could inherently increase the tumour to non-tumour dose ratio in proton therapy.

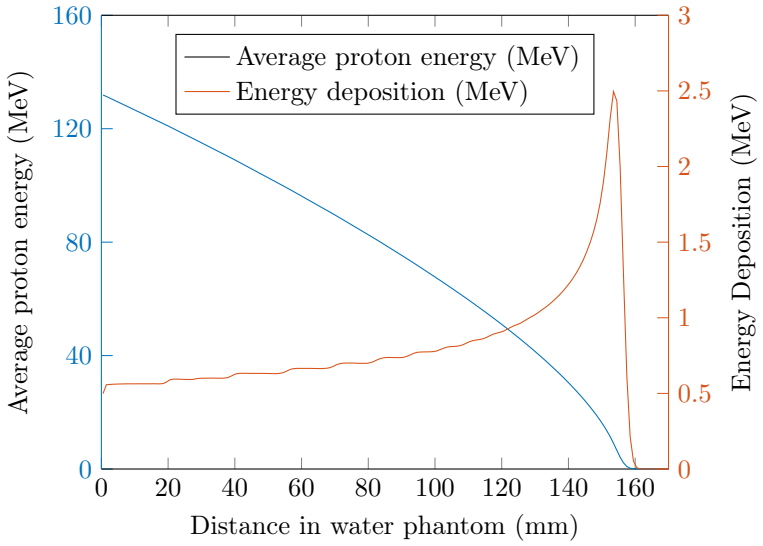

Figure 1.4: The average energy (blue), and the energy deposition (red) of a 140 MeV proton beam, as a function of depth in a water phantom. Data obtained from an MCNP6 simulation.

1.4 Previous research on PBCT

Proton boron capture therapy has been researched since 2014 primarily using simulation, but later in 2018 an experiment has also been performed showing optimistic results [18, 19]. As a reaction to these simulations and experiment, a paper was published by Mazonne et al., disproving any possible dose enhancement due to proton boron capture reactions [20]. This chapter summarizes this apparent contradiction of results.

1.4.1 Monte Carlo simulation results

PBCT has been first studied using MCNPX, and a series of results were published claiming a 50-90% increase in deposited dose in the Bragg peak [21, 22, 18]. The computational geometry used is a 10x10x10cm water phantom, consisting of 0.1mm slabs. An unidirectional proton beam was simulated using 80 MeV primary protons, and the energy deposited by the protons in pure water was compared to simulation using a boron uptake region. This is the boron uptake region (BUR), which is indicated in Figure 1.5 as the yellow area, is the area where boron is present in the system. This boron uptake region was the Bragg peak location ± 5mm. The results are depicted in Figure 1.5, which show a doubling of dose peak height. This peak height insinuates an increase in dose, however dose is not determined by peak height but by the area under the peak, which is not discussed.

1.4.2 Experimental results of PBCT

The first experiments to measure the effectiveness of PBCT were done by Cirrone et al. [19], which studied the cell survival for boronated and non-boronated cultures with and without irradiation. The used boron concentration was 80 ppm, this did not decrease cell survival as was concluded from the cell culture experiment without irradiation. Figure 1.6 depicts a 50 % decrease of cell survival, comparing irradiation of non-boronated cells with boronated cells. The author suggests this decrease in cell survival is the result of the proton boron capture reaction, increasing the dose to the boronated cell cultures.

In response to these promising results published on PBCT, Mazzone et al. [20] performed both analytic calculations and Monte Carlo simulations using Geant4, to reproduce the results of Jung et al. [21], and find a possible explanation for the results of Cirrone et al [19]. The optimistic analytic calculation shows less than 1e-6 alpha particles created per proton, and the simulations

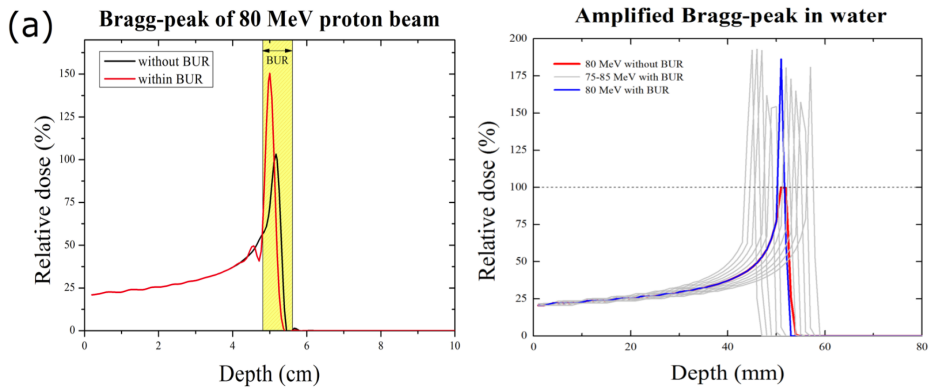

Figure 1.5: Simulation results of previous work done by Yoon et al. [2014] and Jung et al. [2017] using MCNPX. The left and right figures use the same geometry and are produced by the same research group. Source: left [18], right [21].

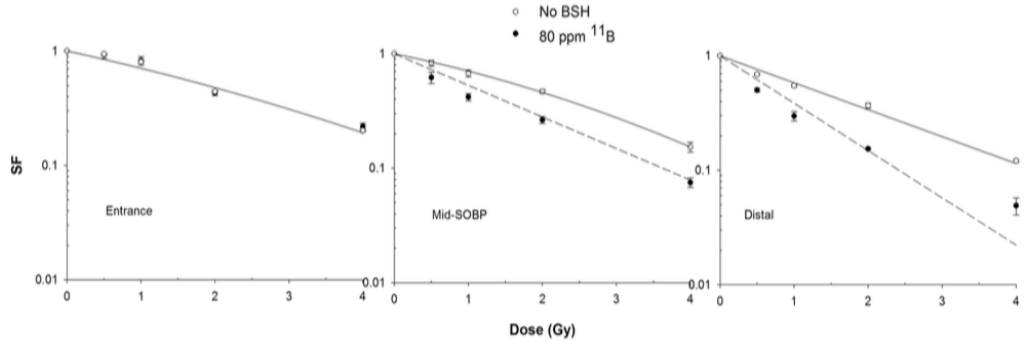

Figure 1.6: Results from the first experiments done on proton boron capture [19]. The shown data refers to dose-response curves obtained at different positions along the spread out Bragg peak.

show a relative dose increase of 1e-7 per proton due to ^{11}B. Thus, Mazzone et al. claim there is no physical foundation for the proton boron capture reaction to enhance proton therapy.

1.5 Research goals

The scientific discussion and varying results obtained in previous research formed the foundation of this thesis. The main goal was to reproduce the published results and to further investigate *the feasibility of proton boron capture therapy*. This was done by:

- Using MCNP6 to reproduce previously observed energy deposition increase (Section 3.1).
- Using Geant4 to check the reproducibility of MCNP6 results (Section 3.2).
- Creating a Boltzmann transport model to investigate reactions not included in the Monte Carlo methods (Chapter 4).
- Conducting a parametric search, using a Boltzmann transport model, to explain the experimental proton boron results (Chapter 5).

2 Monte Carlo methods for proton transport simulation

Doing a simulation study on the feasibility of proton boron capture therapy, requires the simulation of particle transport through a phantom. To investigate possible increases in alpha production during proton therapy, the proton capture rate had to be determined, for all locations from skin to tumour. Therefore, the proton flux as a function of depth in a water phantom was used, the flux can be described as the number of particles moving through a medium in different directions having varying energies. Combining reaction and heating cross sections with the flux can result in reaction rates and energy deposition profiles through the phantom [23]. This flux can be determined using the Monte Carlo method, which utilizes repeated random sampling to obtain numerical results, which are the expected value and variance of a series of coupled distributions. More specifically, this thesis made use of MCNP6 and Geant4 Monte Carlo methods for simulation of coupled proton alpha transport.

2.1 Monte Carlo method for average flux estimation

To apply Monte Carlo methods to particle transport, the system has to be defined, which is a geometry consisting of cells. Each cell consist of a material, which should have cross section data available. The cross section database is a collection of descriptions of the probability and consequence of interactions. If cross section data is not available, nuclear models can be used to create cross sections. A particle source is defined to initiate the simulation of transport.

To determine the total trail or history of one particle, its "life" needs to be tracked. First, the direction and energy of the source particle are sampled from the distribution specified by the user. The path between the current and the next position is the distance traveled by the particle, without collision or change in energy. This path is determined using the total cross section of the material for the particle being transported. Subsequently, the particle is transported to this next position. At this position, the particle can either scatter or be absorbed, scattering will results in energy loss and a possible change of direction. Absorption may result in a nuclear reaction, that can cause the creation of secondary particles, which will also be tracked. These particles have a starting energy sampled from the reaction data, the transport is simulated equivalently to source particles. Not tracking these particles results in all particle energy deposited locally to maintain energy conservation. Sampling new positions for a particle can continue until a cut-off is reached, which can be based on minimal energy of the particle or a maximal number of steps for one history. However, the sampling can also stop if the particle is absorbed or transported to a cell outside of the geometry.

This process is repeated for a large number of trials, called histories or random walks. This repeated random sampling does not have any value by itself, but scoring is applied to obtain flux or flux-related quantities. The scoring is performed during the random walk, after which the scores obtained are averaged. The estimated average scores and their statistical relative errors (r.e.) are kept in a tally. The relative error is inversely related to the square root of the number of histories N. That is,

$$r.e. \propto \frac{1}{\sqrt{N}}. \tag{2.1}$$

The average volume flux can be determined by Monte Carlo methods using a track length estimator. The average volume flux tally, sums over the path lengths s_i each particle has trough volume V and accumulates this (see Figure 2.1). Afterwards, the average flux ϕ_V is estimated as

$$\overline{\phi_V} \simeq \frac{1}{NV} \sum_{i=1}^{N} \sum_{j=1}^{n_i} s_i^j, \tag{2.2}$$

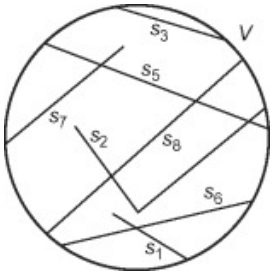

Figure 2.1: Particle paths through volume V. Source:[24]

with N being the total number of histories, n_i is the number of times particle i passes through volume V with s_i^j being the path lengths in pass j [24]. The unit by which the average volume flux is described is particles per cm^{-2} per source particle.

This flux tally can be split up in bins of energy, by integrating over the width of the energy bin ΔE, using the integral

$$\int_E \phi(\boldsymbol{r}, E) dE, \tag{2.3}$$

where $\phi(\boldsymbol{r}, E)$ is space ($\mathbf{r}$) and energy (E) dependent steady state flux, determined by a flux tally. Energy bins can be used to multiply the flux with an energy dependent factor, this was utilized to determine reaction rates in Chapter 4.

2.2 Monte Carlo energy deposition and reaction rate calculation

The previous section described how to determine the flux at different sections within the geometry. Here we show how energy deposition and reaction rate are calculated using this flux. More specifically, the reaction rates are determined using a cross section database, which contains all information on the interaction chance and consequence for a set of isotopes. This tabulated data is used to determine which interaction happens within each cell in the geometry. These cells consist of a material that can be described by a mixture of isotopes from the cross section database.

Equation 2.4 displays the integral to be solved for each cell within the geometry to determine the reaction rate. This integral yields the reaction rate R_σ in a cell as reactions per cm^3 per source particle:

$$R_\sigma(cell) = \int_E \int_{\boldsymbol{r} \in \boldsymbol{cell}} \rho_n(\boldsymbol{r}) \sigma(E, \boldsymbol{r}) \phi(\boldsymbol{r}, E) d\boldsymbol{r} dE, \tag{2.4}$$

where ρ_n is the number density of the material at $\mathbf{r}$, σ is the microscopic cross section (cm^{-2}), and is retrieved from tabulated data. The unit of the reaction rate is number of reactions per cm^3 per source particle. This cross section is material and energy dependent. The reaction rate can be used to determine the production rate of secondary particles, using only the flux and the cross section. This can be used to determine the alpha particle production rate increase.

To determine the feasibility of proton boron capture therapy a measure of cell killing potential is needed. Therefore a dose tally is used to measure the absorbed dose D. Dose can be described as energy deposited per unit mass, hence equation 2.5 is used to determine the energy deposition:

$$E_d = \rho_a \int_E \int_{\boldsymbol{r}} H(E) \phi(\boldsymbol{r}, E) d\boldsymbol{r} dE, \tag{2.5}$$

$$D = \frac{E_d}{V \rho_g}. \tag{2.6}$$

Energy deposition is in units of MeV and absorbed dose D in MeV/g. The densities ρ_a and ρ_g are the atomic and mass densities respectively. For each position $\mathbf{r}$ the flux ϕ is multiplied by the

heating number H. For charged particles this heating number is strongly related to the stopping power, which is defined as the total energy loss per unit distance.

2.3 MCNP6 Monte Carlo code

MCNP is a general Monte Carlo N-Particle transport code developed by Los Alamos National Laboratory, University of New Mexico. This original Fortran 90 code was developed for describing neutron and photon transport, with neutral particle transport being the main focus. For charged particle transport, the extended MCNPX was developed. While MCNPX and MCNP5 co-existed, later these two versions were merged together to form MCNP6. The version used for this thesis was MCNP6.2.

MCNP6 is a code used by providing MCNP6 with an input file, subsequently MCNP6 generates the output file. The input file is split up in cards that have different functions. The input file is used to describe the cells that make up the geometry, by using the surfaces and the materials described in the same file. Also, control of simulation parameters is done via this card e.g. the energy cut-off for particles, the source particle energy and direction distribution, tallies, number of histories and more. For a full explanation of all options controllable see the MCNP6 manual [25]. For an example of an input file used see Appendix A. The output file contains information for all particles chosen to be tracked, which is summarized at the start of an output file. This summary contains information about how many particles per particle type are created and lost, how they are created and lost (e.g. capture, source or escape geometry) and the particle energy created or lost. Additionally the results of requested tallies are displayed in this file. Tallies used in this thesis are described in Table 2.1.

Table 2.1: Short description of MCNP6 tallies used in this thesis. For a more detailed description see [25].

Tally name	**Description (*unit*)***
F4	The volume flux tally, average track length divided by the volume. $(\#/cm^2)$
F6	The energy deposition tally, the flux multiplied by the heating number. (MeV)**
FM4	Flux multiplier, can be used to multiply the flux by any constant or cross section. This tally was used to determine the reaction rates. $(reactions/cm^3)$**
E4	Energy bin tally. Used to divide a flux tally in energy bins.

*All units are per starting particle.
**One of the possible units.

The flux multiplier tally (FM) is used to multiply a particle flux by a constant, or an energy dependent cross section. Using the energy dependent reaction cross section for each cell in the geometry the reaction rate can be determined. The FM tally is used by supplying MCNP6 with a reaction number, corresponding to the reaction rate of interest. Proton reaction numbers used by MCNP6 are not equivalent to the neutron reaction numbers. For neutron reactions, the standard ENDF6 format number can be used [26]. For protons, not all reaction can be tallied, and the reaction numbers are based on the secondary particle produced during reaction. The flux has to be multiplied by both the total reaction number and the secondary particle reaction number. This is described differently in the MCNP6 manual, normally for an FM tally the flux should only be multiplied using the secondary particle reaction number. However while using the new TENDL2017 cross section library, an FM tally with the correct reaction number, resulted in MCNP6 multiplying the flux by the secondary particle yield, which is the fraction of the total reaction cross section producing these secondary particles. Therefore, both the specific secondary particle reaction number and the total reaction number had be multiplied by the flux to obtain correct reaction rates.

2.4 Geant4 Monte Carlo code

Geant4 is a toolkit for simulating particle transport through matter. Whereas this toolkit has initially been developed by CERN in 1993 to simulate high energy hadron physics, Geant4 is currently applied in many other physics fields. Geant4 is a C++ toolbox which can be used to develop custom applications, with functionalities such as tracking, geometry, physics models and hits [27]. For proton therapy, the Geant4 based framework GATE is used for treatment planning. The multiple coulomb scattering models, important for proton range, have been verified to be accurate in Geant4 [28].

Geant4 is used together with MCNP6, to obtain a stronger foundation for the results obtained through Monte Carlo simulation. While both MCNP6 and Geant4 are Monte Carlo methods for simulating particle transport, they are not used the same. Geant4 can be used to build complete application, like GATE, while only using the functionalities of Geant4. When using Geant4 more on basic level, the use of example applications provided at the Geant4 website [29] is advised.

3 Monte Carlo simulation of PBCT using MCNP6 and Geant4

To determine the effect of boron capture during proton therapy, Monte Carlo simulation was used. This method was used because in previous research by Jung et al., it had proven to be an effective tool to simulate the effect of proton boron capture [21, 22, 18]. First, MCNP6 was used to mimic the simulation and experiments done in previous research. Geant4, an additional Monte Carlo simulation toolkit, was used to validate the MCNP6 results.

3.1 MCNP6 simulations

3.1.1 Model details: geometry and settings

The used version of MCNP was MCNP6.2, obtained from Los Alamos National Laboratory, Los alamos, New Mexico. The default MCNP6.2 cross section library was extended by adding the TENDL2017 proton cross section file [30]. This was needed because the default cross section database did not contain the proton + ^{11}B reaction. For the non-proton interactions the default MCNP6.2 cross sections were used, which is the ENDF/B-VIII.

The simulation used a box shaped phantom geometry. The phantom was surrounded by a vacuum. The proton beam was directed along the x-axis in the center of the box. Figure 3.1 shows this geometry. The size of the box was ensured to be big enough to prevent protons escaping the back of the phantom. The material of the phantom was $^{1}H_2{}^{16}O$ with a determined concentration ^{11}B added. This boron was added only in the Bragg peak area for mimicking the Jung et al. simulation [21] and is distributed uniformly over the phantom for all other simulations. The proton boron capture reaction only dominates the alpha production in the Bragg peak. Therefore, the distribution of boron should not matter for the dose increase caused by the capture reaction.

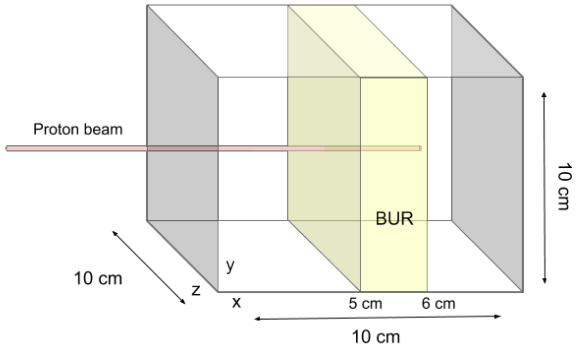

Figure 3.1: The geometry used for the simulation. Both for MCNP6 and Geant4 this same geometry was used. The yellow area indicates a boron uptake region (BUR)

During simulation all secondary particles were tracked using the MODE card for protons, neutrons, photons, electrons and alpha, tritium, deuterium, and ^{3}He particles. The energy cut-off was set to 1 keV for alpha, tritium, deuterium, and ^{3}He particles, while for protons the cut-off was set to 0.1 MeV. For neutrons, electrons and photons the cut-off was not changed from the default value of 1 eV. For protons the maximum proton energy was set to 200 MeV using the PHYS:H card, all other settings were default. Simulations were done using 2e6 source protons with the same initial energy, which were directed along the x-axis starting at x, y, z = 0. For an example of an input file refer to Appendix A.

The flux, energy deposition and reaction rate in the phantom were determined in slabs of 1 mm along the x-axis. The tallies used were F4, F6, FM4 and E4 to determine the flux and reaction rates for each slab. For details on these tallies, see Section 2.2. The total energy deposition is the sum of the energy deposited by the proton and the RBE corrected energy deposited by secondary alpha particles. For this RBE correction the energy deposition tally results for alpha particles are multiplied by a factor 20 to correct for higher biological effectiveness of this deposited energy. For protons an RBE of 1.1 can be used, however for this thesis the proton energy deposition is not RBE corrected, since this 1.1 will not considerably affect the proton boron capture feasibility.

3.1.2 Results

To reproduce the results obtained by Jung et al., exactly the same dimensions were used as described in their paper [21]. The water phantom size was 10 x 10 x 10 cm, the source energy of protons energy was 80 MeV, and the boron concentration was 1.04mg/g (1710 ppm) of pure ^{11}B. The boron was only present in the boron uptake region (BUR). The BUR was aligned with the Bragg peak and had a width of 10 mm, covering the region from 50 to 60 mm in the phantom. The result depicted in Figure 3.2 shows a negligible energy deposition difference for ^{11}B addition to the system. A small peak shift can be observed towards the beam entrance, while the total energy deposition (=area under energy deposition graph) does not change. This peak shift can be contributed to a small density change caused by the ^{11}B, not due to alpha particle production.

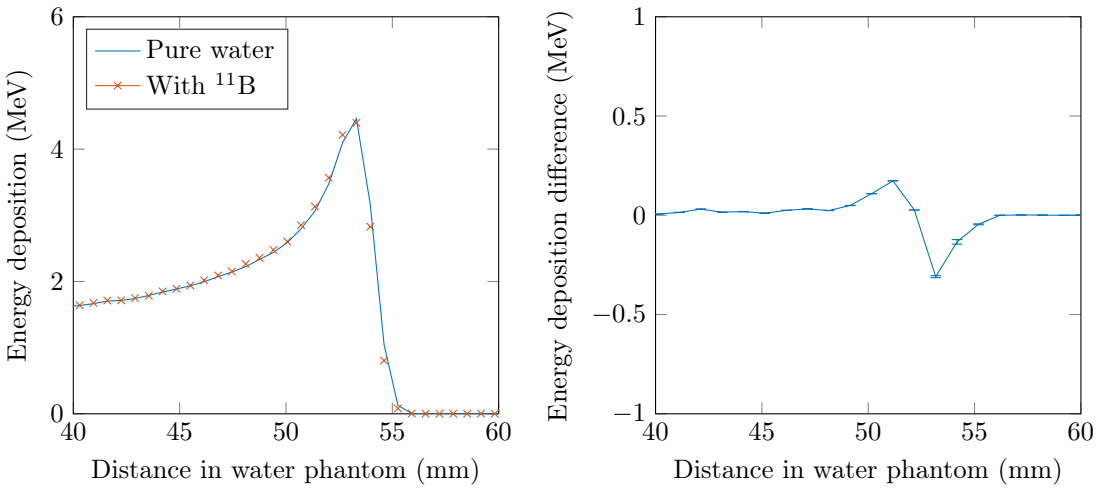

Figure 3.2: Attempt at reproducing results from Jung et al. [21]. The left figure shows the energy deposition curves, for pure water and for water with a boron uptake region from 50 to 60 mm. The right figure shows the difference between these two curves. The total energy deposited is the same for the two curves, however the right figure shows a small peak shift towards the beam entrance. The total energy deposition difference is negligible. The error bars in the right figure are the statistical errors calculated by MCNP6. The left figure has a r.e. $<$ 1e-3, therefore these are not shown in the figure.

To further investigate the possibility of dose enhancement, simulations were performed over the energy range of 75 MeV to 200 MeV with increments of 25 MeV. This upper limit was chosen because the TENDL2017 library was only available up to 200 MeV. The concentration of ^{11}B was 100 ppm as used in the promising experiments by Cirrone et al. [19]. Table 3.1 shows the energy deposition change relative to the deposition in pure H_2O. The result is statistically not significantly different from zero, due to high error margins and low values. The maximum value found was an increase of 13.4 keV, which is three orders of magnitude smaller than the energy deposited by the proton.

Table 3.1: For primary proton energies ranging from 75 MeV to 200 MeV the energy deposition change inside the Bragg peak, relative to the deposition in pure H_2O. The errors given are absolute, and represent the MCNP statistical error.

Primary proton Energy (MeV)	Energy deposition difference at Bragg peak (MeV ± MeV)
75	4.64e-3 ± 1.90e-2
100	-9.28e-3 ± 2.20e-2
125	-6.40e-3 ± 3.05e-2
150	1.56e-3 ± 3.44e-2
175	1.34e-2 ± 2.78e-2
200	-2.16e-2 ± 4.51e-2

3.1.3 Secondary neutron ^{10}B reaction rate

Research done by Mazzone et al. [20] stated that the proton - ^{11}B reaction could not have caused the increase in cell death found in the experimental work. This conclusion was based on basic analytic calculations, and the authors suggested a different mechanism had to be the cause of the decreased cell survival. The hypothesis was that, secondary neutrons reacting with ^{10}B resulting in release of high LET alpha particles [31] were responsible for the higher cell death. The same reaction is utilized for BNCT (see Section 1.3.1), the ^{10}B(n,α) reaction.

This capture reaction is suggested, since the boron used to conduct the experiments was natural boron (80%^{11}B and 20%^{10}B), and secondary neutrons are present in the system due to proton ^{16}O capture reactions. The secondary neutrons sources are the ^{16}O(p,n+p) and ^{16}O(p,2n+2p) reactions, both having a cross section of approximately 100 mb in the therapeutic proton energy range.

The neutron ^{10}B capture reaction has a high cross section (3740 barn) [13], however this is only valid for low-energy thermal neutrons. As seen in Figure 3.3, this neutron capture cross section decreases with increasing energy of the neutrons. Therefore, the average secondary neutron energy was tallied, which was done using MCNP6 simulation of a proton beam in water with 1000 ppm of natural boron. This simulation was done using a 10 x 10 x 10 cm box divided in slabs of 1 mm. The average secondary neutron energy at creation was determined from the MCNP6 output summary. This resulted in an average secondary neutron energy of 15 MeV. For this energy the cross section was around 0.1 barn. To determine the reaction rate for neutron ^{10}B capture, an FM tally was used to multiply the neutron flux by the macroscopic energy dependent cross section of 1000 ppm of natural boron in water. This reaction rate was in the order of 1e-5 reactions/cm^3 per incoming proton, and did not vary over the length of the phantom.

3.2 Geant4 simlulations

Because MCNP6 was not able to reproduce the results obtained in previous research by Jung et al. [21], Geant4 was used to investigate whether an other Monte Carlo method could reproduce these results, and to check if the results would be similar to the results found in Section 3.1.

3.2.1 Model details: geometry and settings

The used version of Geant4 was Geant4-10.4.2, which was obtained from the official Geant4 website [29]. The default cross sections from Geant4 were used. The extended example Hadr01 was used as a basis for simulation [32]. This example tracks source protons through a geometry and tallies flux, energy deposition, and energy distribution. The only changes made to the example were the addition of custom materials, which were different concentrations of ^{11}B in water. QGSP_BIC_HP and emstandard_opt4 were the physics lists used, which are recommended for medical applications. For particle cut-off 10 nm was adopted. The geometry used was identical to the MCNP6 geometry (see Figure 3.1). Slabs of 1 mm were used and for each slab the energy deposited was scored. Each simulation used 2e6 source protons.

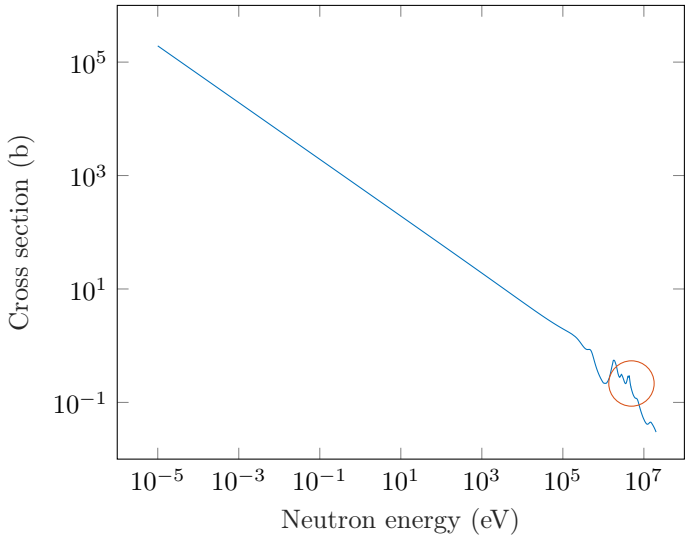

Figure 3.3: The cross section of neutron capture by ^{10}B. The red circle indicates the average secondary neutron energy during proton therapy.

To check the reproducibility of the results obtained by using MCNP6 in Section 3.1, the Geant4 geometry was again a 10 x 10 x 10 cm phantom, consisting of 1 mm slabs in the x direction. The BUR was aligned with the Bragg peak, covering the region from 45 to 55 mm in the phantom. This varies from the MCNP6 (50 - 60 mm), because the Bragg peak was located more towards the beam entrance for the Geant4 simulation.

3.2.2 Results

The results shown in Figure 3.4 depict only an energy deposition peak shift toward the beam entrance. This peak shift was due to density increasing effects and no net increase in energy deposition is found.

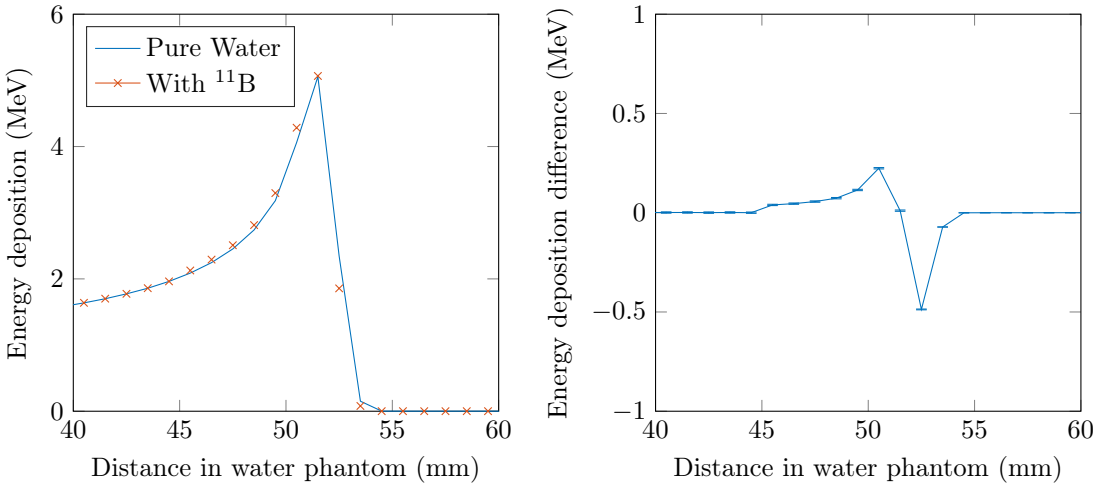

Figure 3.4: Results from Geant4 simulation using parameters used by Jung et al. [21]. The right figure shows the energy deposition curve, for a pure water phantom, and for a water phantom including a BUR from 45 to 55 mm. The right figure shows the difference between these two curves, a shift toward the beam entrance of the peak is seen. The total energy deposited remains unchanged with addition of ^{11}B. The shown error bars are the statistical errors calculated by Geant4. The left figure has a r.e. $<$ 1e-3, therefore these are not shown in the figure.

Figure 3.5 compares the Geant4 results to the MCNP6 results, similarly showing the peak shifting effect. These peak shifts have no effect on the total deposited energy in the phantom.

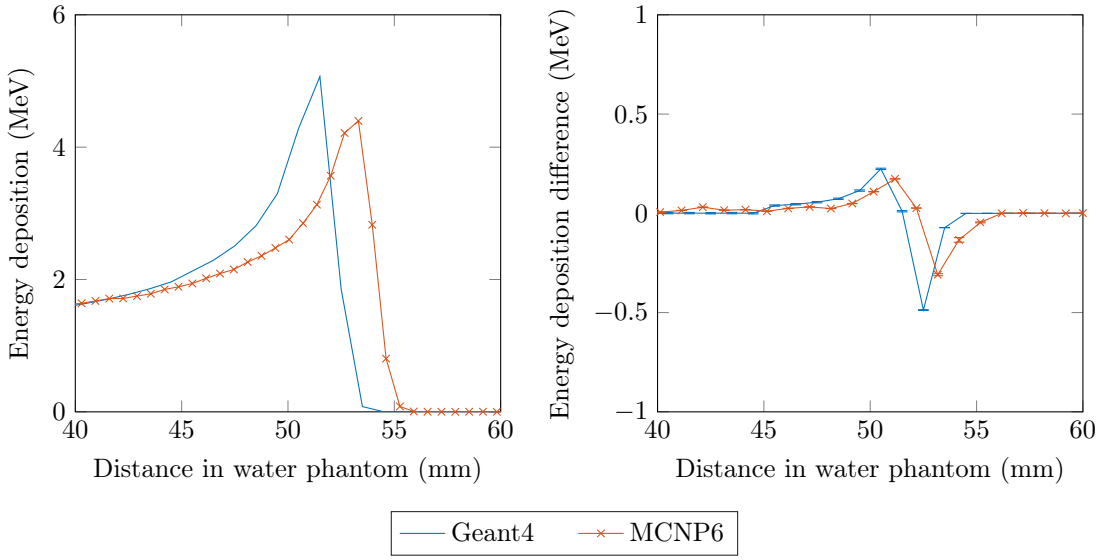

Figure 3.5: The energy deposition profile for Geant4 and MCNP6 with ^{11}B from Figures 3.4 and 3.2 (left). From the same figure the energy deposition difference from is depicted (right). The profiles are similar but the location of the peak is shifted towards the beam entrance.

3.3 Discussion

The proton boron capture simulation performed with Geant4 showed minimal increase in energy deposited. This could be attributed to Geant4 using the ENDF-VIII.0 cross section database, which does not include the proton ^{11}B capture reaction.

Equivalently, the MCNP6 simulations did not show a significant increase in energy deposition, however the proton ^{11}B capture reaction cross section (TENDL2017) was included. As seen in Figure 3.6, the alpha production for boron is orders of magnitude lower than for oxygen. Moreover, only at the end of the Bragg peak does the oxygen alpha production goes to zero. For the investigated concentrations (100 - 1710 ppm) in Section 3.1, the ^{11}B alpha production rate was negligible compared to the oxygen reaction rate. At the Bragg peak location, the ^{11}B microscopic cross section is three times higher than the oxygen cross section, however the oxygen concentration ($\sim$1e6 ppm) is thousand times higher than the boron concentration (1e3 ppm). Therefore, the resulting ^{16}O production rate was three hundred times higher.

To explain the results of Jung et al. the research group has been contacted. More details about the simulations, that were not described in the papers published by this research group, were discussed. One interesting detail was the density inside the BUR, which for simulations done by the research group was set to the density of natural boron. To reproduce these results a simulation was done for pure water, and a simulation where the density of water was set to the density of natural boron (2.07 g/cm^3), but without adding any boron. Figure 3.7 shows the energy deposition peak is twice as high in the BUR compared to pure water. This peak height increase was due to an increase of the density of the "boron" uptake region to twice the density of water, which resulted in a higher and sharper Bragg peak. The total energy increase does not change with addition of this BUR because the peak is not only twice as high but also twice as small, resulting in the same total energy deposition. Figure 1.5 shows the results obtained in previous research [21, 18], also obtaining the higher, but less broad peak, resulting in no effective energy deposition increase.

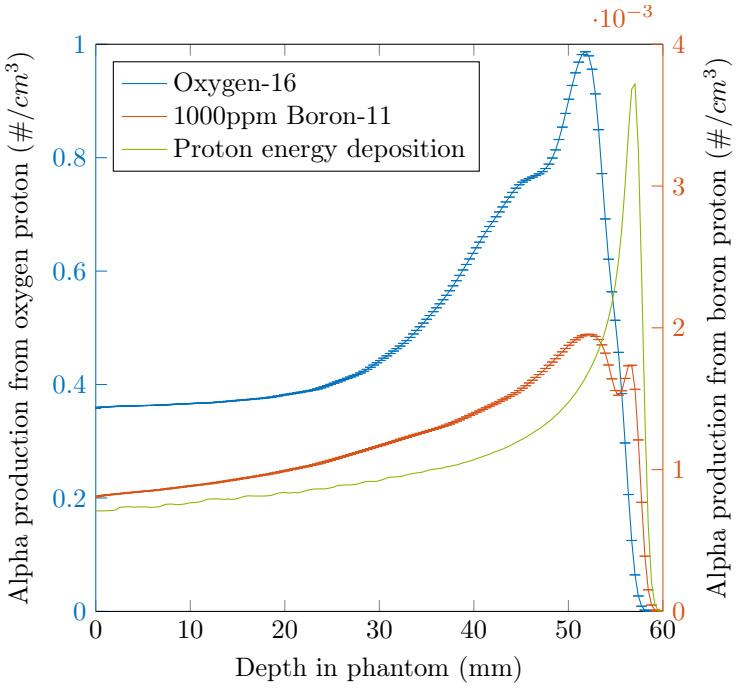

Figure 3.6: The production of alpha particles for ^{16}O and ^{11}B as a function of location. The energy deposition (green) of a proton shows a clear Bragg peak profile (a.u.). The production of alpha particles in the Bragg peak goes to zero for oxygen but the peak for boron is low (three hundred times lower). The Bragg peak shown has no units and is shown as a location indicator.

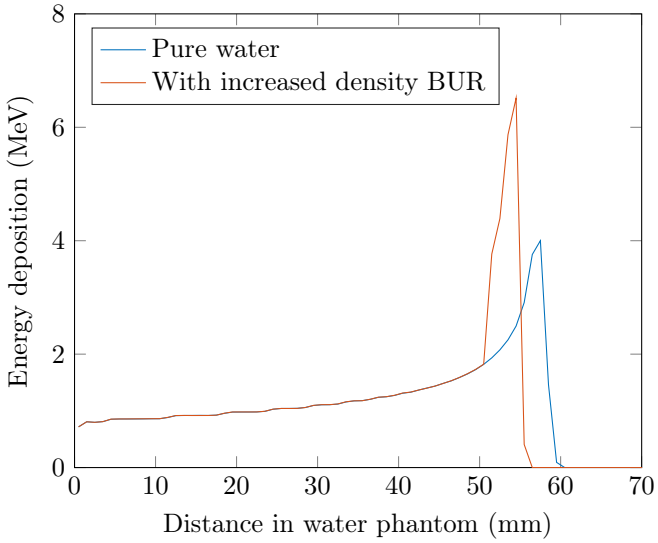

Figure 3.7: The energy deposition profile for protons in pure water, which were obtained by simulation using MCNP6. The energy deposition is compared for pure water and for pure water having the density of natural boron (2.07 g/cm^3) from 50 - 60 mm. The energy deposition peak is twice as high but the total energy deposition is the same, since the peak is half the width.

4 Modelling proton boron capture using simplified Boltzmann equations

As explained in the previous chapter, certain reaction cross sections that could cause a higher alpha production are not available in MCNP6 or Geant4. These missing cross sections are proton boron capture below 1 MeV and the alpha-proton-alpha avalanche reaction (see Section 4.4). This chapter will describe how these reactions and the resulting dose increase are modelled.

First, it is necessary to model the transport of protons and alpha particles. For this purpose, a set of simplified linear Boltzmann equations is used, which are one dimensional (Section 4.1). Second, the proton flux equation was split in three equation for the energy bins ranging from 80 to 7 MeV, 7 to 2 MeV and 2 to 0.5 MeV. Subsequently, the currently available cross sections are obtained from MCNP6 data (Section 4.2). With only these available cross sections, the steady state flux resulting from this model matched the MCNP6 flux (Section 4.3). Finally, the proton boron capture below 1 MeV, and the alpha-proton-alpha avalanche reaction cross sections were added to the model (Section 4.4). Due to the time dependent nature of the avalanche reaction [33], time dependence was added to the model. The resulting dynamic model is described to explore non-steady state dose effects (Section 4.5).

4.1 Simplification of the linear Boltzmann transport equation

A Boltzmann equation describes the behaviour of a system which is not in thermodynamic equilibrium. The linear Boltzmann transport equation (LBTE) is derived from this equation with the assumption that the transported particles interact with the medium they travel through, but not with one another. Equation 4.1 [34] defines the Boltzmann transport equation used as the basis for the simplification steps.

$$\Big[\overbrace{\frac{1}{v}\frac{\partial}{\partial t}}^{a}+\overbrace{\hat{\boldsymbol{\Omega}}\cdot\nabla}^{b}+\overbrace{\Sigma_t(\boldsymbol{r},E,t)}^{c}\Big]\phi(\boldsymbol{r},E,\hat{\boldsymbol{\Omega}},t)= \underbrace{\int_0^\infty dE'\int_{4\pi}d\hat{\boldsymbol{\Omega}}'\Sigma_s(\boldsymbol{r},\hat{\boldsymbol{\Omega}}'\rightarrow\hat{\boldsymbol{\Omega}},E'\rightarrow E)\phi(\boldsymbol{r},E',\hat{\boldsymbol{\Omega}}',t)}_{d}+\underbrace{s(\boldsymbol{r},E,\hat{\boldsymbol{\Omega}},t)}_{e}. \quad (4.1)$$

This transport equation consists of five terms, with ϕ being the flux ($\#/cm^2s$). The first term on the left-hand side (a) is the partial derivative of flux with respect to time (t in seconds), and v is the velocity of the particles (cm/s). The second term (b) is the streaming of particles, ∇ is the spatial gradient, and $\hat{\boldsymbol{\Omega}}$ is the angle of motion. The last term on the left-hand side (c) is the total macroscopic removal cross section (cm^{-1}) of the material, which consists of the capture and outscattering cross section. The first term on the right hand side (d) refers to the inscattering of particles, which is the gain of particles into energy E and direction $\hat{\boldsymbol{\Omega}}$ from energies E' and directions $\hat{\boldsymbol{\Omega}}$'. The extent of inscattering is governed by the scatter cross section Σ_s. The final term (e) is added for completeness, and refers to the external source term ($\#/cm^3s$).

To use this equation for simple proton and alpha particle transport, various modifications were made. First the protons used for simulation are accelerated only in the x-direction, the created alpha particles will generally move in this similar direction. Therefore, the assumption is made that all fluxes are mono-directional parallel to the x-axis, removing angular dependence. Second, the flux was assumed to have no width, hence being one dimensional. These two assumptions reduce Equation 4.1 to:

$$\Big[\overbrace{\frac{1}{v}\frac{\partial}{\partial t}}^{a}+\overbrace{\frac{\partial}{\partial x}}^{b}+\overbrace{\Sigma_t(x,E,t)}^{c}\Big]\phi(x,E,t)=\overbrace{\int_0^\infty dE'\Sigma_s(x,E'\to E)\phi(x,E',t)}^{d}+\overbrace{s(x,E,t)}^{e}. \quad (4.2)$$

4.1.1 Source term characterization

The source term (e, in Equation 4.2) is zero for protons, no external source term is present in the system. Alpha particles however are created by the nuclear reaction of protons with ^{16}O and ^{11}B, which are:

$$p+{}^{16}O\to\alpha+{}^{13}N \quad and \quad p+{}^{11}B\to 3\alpha.$$

The cross sections for these reactions multiplied by the proton flux is the resulting source term for alpha particles. This source term for alpha particles is added to Equation 4.2 to obtain the alpha flux equation:

$$\Big[\frac{1}{v_\alpha}\frac{\partial}{\partial t}+\frac{\partial}{\partial x}+\Sigma_{t,\alpha}(x,E,t)\Big]\phi_\alpha(x,E,t)=\int_0^\infty dE'\Sigma_{s,\alpha}(E'\to E)\phi_\alpha(x,E',t)+ \chi(E)\int_0^\infty[\Sigma_B(x,E',t)+\Sigma_O(x,E',t)]\phi_p(x,E',t)dE', \quad (4.3)$$

where the subscript p is used for proton and the subscript α for alpha particles. Σ_O (cm^{-1}) is the ^{16}O cross section for protons being captured and producing one alpha particle. Σ_B (cm^{-1}) is the ^{11}B cross section for capturing a proton and producing three alpha particles, a multiplicity which is included in the cross section. The alpha particles according to energy spectrum $\chi(E)$.

4.2 Energy bin and cross section characterization

4.2.1 Energy bin characterization

The aim of creating this model was to investigate the effect of proton boron capture below 1 MeV, which can be accomplished by dividing the proton flux in three energy bins. The highest energy bin varies from 80 MeV, the incoming proton energy, to 7 MeV, the energy below which protons stop reacting with ^{16}O (see Figure 1.3). The next energy bin runs from 7 to 2 MeV and the lowest from 2 to 0.5 MeV. This 2 MeV, and not exactly 1 MeV, is chosen to overestimate the effect of the increase in alpha particle production. The alpha flux source term in Equation 4.3 can now include all three proton fluxes with their respective cross sections, which will be individually adjusted. Accordingly, the lowest energy bin proton-^{11}B cross section can be increased to include the proton capture below 1 MeV.

Below 0.5 MeV protons do not have enough energy to react with ^{11}B. Therefore, this energy was chosen to be the cut-off energy, if protons reach the cut-off energy they are no longer tracked as being part of any flux. For alpha particles a cut-off energy of 1 MeV was chosen, below this energy the alpha-proton acceleration (see Section 4.4) can not result in protons with an energy higher than 0.5 MeV. Below the cut-off energy all residual energy is deposited locally, to preserve total energy conservation.

Splitting up the proton flux resulted in three proton equations and one alpha particle equation, these four equations are simplified by neglecting upscatter and not including self scatter. Upscatter is a scattering event resulting in a particle gaining enough energy to move up an energy bin. Self scatter is described as a scattering event, which does not result in enough energy change to move outside of the current energy bin. Self scatter could be added to both sides of the equations and is therefore not included. Consequently all scatter events are outscattering events. To define the outscatter cross section the total removal cross section is split into a nuclear capture cross section Σ_c, which is defined as a particle being removed due to nuclear capture, and the outscatter cross section Σ_s:

$$\Sigma_t = \Sigma_s + \Sigma_c.$$

An outscatter event causes the particle to lose enough energy to go down one or more energy bins. For alpha particles and the lowest energy bin protons, this outscatter cross section is used to determine the fraction of the flux reaching the energy cut-off. The inscattering term (d) from Equation 4.2 for each energy bin will be equal to the outscatter coming from higher energy bins. For the alpha flux (Equation 4.3) and all proton energy bins the inscatter term will be described as:

$$\begin{aligned}
&\text{(Alpha)} && \int^{\infty} dE' \Sigma_{s,\alpha}(E' \to E)\phi_{\alpha}(x,E',t) = 0, \\
&\text{(80 to 7 MeV bin)} && \int_{80}^{\infty} dE' \Sigma_{s,p}(E' \to E)\phi_{p}(x,E',t) = 0, \\
&\text{(7 to 2 MeV bin)} && \int_{7}^{80} dE' \Sigma_{s,p}(E' \to E)\phi_{p}(x,E',t) = \Sigma_{s,80\to 7}(x,t)\phi_{p,80}(x,t), \\
&\text{(2 to 0.5 MeV bin)} && \int_{2}^{80} dE' \Sigma_{s,p}(E' \to E)\phi_{p}(x,E',t) = \Sigma_{s,7\to 2}(x,t)\phi_{p,7}(x,t) \\
& && \qquad + \Sigma_{s,80\to 2}(x,t)\phi_{p,80}(x,t).
\end{aligned}$$

The flux in the equation has the subscripts of the corresponding energy bin and particle type ($\phi_{\text{particle type, energy bin}}$). For the scattering cross section, the subscripts describe the outscatter energy group and the inscatter energy group, e.g. $\Sigma_{s,80\to 7}$ represents the cross section for scatter from the 80 to 7 MeV proton energy bin to the 7 to 2 MeV bin. For the alpha flux equation and the highest energy bin proton equation the inscatter will be zero, since no higher energy bin exists and selfscatter is neglected. The inscatter part of the alpha source term is zero, the second alpha source term was integrated over the energy bins

$$\chi(E)\int_0^{\infty}[\Sigma_B(x,E',t) + \Sigma_O(x,E',t)]\phi_p(x,E',t)dE' = \Sigma_{B,2}\phi_{p,2}(x,t) + \Sigma_{B,7}\phi_{p,7}(x,t) + [\Sigma_{B,80} + \Sigma_O](x,t)\phi_{p,80}(x,t). \quad (4.4)$$

Equation 4.4 is the total source term for the alpha flux equation, this term uses four cross sections to determine the alpha production. The proton-^{11}B reaction cross section is split into $\Sigma_{B,2}$, $\Sigma_{B,7}$ and $\Sigma_{B,80}$. These cross sections represent the reaction cross section for proton energies from 0.5 to 2 MeV, 2 to 7 MeV and 7 to 80 MeV. The Σ_O is used to describe the alpha creating reaction cross section of protons with ^{16}O. With the total cross section split up and the inscattering defined, the four equation are described by Equation 4.5 - 4.8:

$$\Big[\frac{1}{v_{p,80}}\frac{\partial}{\partial t} + \frac{\partial}{\partial x} + \Sigma_{s,80}(x,t) + \Sigma_{c,80}(x,t)\Big]\phi_{p,80}(x,t) = 0 \quad (4.5)$$

$$\Big[\frac{1}{v_{p,7}}\frac{\partial}{\partial t} + \frac{\partial}{\partial x} + \Sigma_{s,7}(x,t) + \Sigma_{c,7}(x,t)\Big]\phi_{p,7}(x,t) = \Sigma_{s,80\to 7}(x,t)\phi_{p,80}(x,t) \quad (4.6)$$

$$\Big[\frac{1}{v_{p,2}}\frac{\partial}{\partial t} + \frac{\partial}{\partial x} + \Sigma_{s,2}(x,t) + \Sigma_{c,2}(x,t)\Big]\phi_{p,2}(x,t) = \Sigma_{s,7\to 2}(x,t)\phi_{p,7}(x,t) + \Sigma_{s,80\to 2}(x,t)\phi_{p,80}(x,t) \quad (4.7)$$

$$\Big[\frac{1}{v_{\alpha}}\frac{\partial}{\partial t} + \frac{\partial}{\partial x} + \Sigma_{s,\alpha}(x,t) + \Sigma_{c,\alpha}(x,t)\Big]\phi_{\alpha}(x,t) = \Sigma_{B,2}\phi_{p,2}(x,t) + \Sigma_{B,7}\phi_{p,7}(x,t) + [\Sigma_{B,80} + \Sigma_O](x,t)\phi_{p,80}(x,t) \quad (4.8)$$

Equation 4.5 represents the simplified Boltzmann equation for proton energy bin 80 to 7 MeV, Equation 4.6 the 7 to 2 MeV bin and lastly, Equation 4.7 is for the lowest proton energy bin (2 to 0.5 MeV).

4.2.2 Cross section characterization

To solve Equations 4.5 - 4.8, the cross sections had to be determined. To reduce the number of variables, these cross sections were determined for one geometry and one proton energy using MCNP6. A simulation was done for 80 MeV protons, in a homogeneous phantom consisting of $^{1}H_{2}^{16}O$ with 100 ppm of ^{11}B. The phantom is 10x10x10 cm and consists of 1000 slabs of each 0.01 cm. The proton flux was split up in the energy bins described in the previous section, and the alpha flux was defined as one energy bin ranging from 20 to 1 MeV. For each bin and at each slab position in the phantom, the following was tallied:

ϕ_p and ϕ_α	= Flux (F4)
RR_{tot}	= Total nuclear reaction rate (FM4, MT5)
$RR_{p\to p}$	= Proton producing reaction rate (FM4, MT9005)
$RR_{p\to\alpha}$	= Alpha producing reaction rate for H_2O and ^{11}B separately. (FM4, MT34005)

These tallies were used to determine the nuclear capture cross section for each proton energy bin. For each position the total reaction rate was tallied and divided by the flux, this will result in the total nuclear capture cross section, however this will also include nuclear capture followed by the release of a proton. To overcome this, the total proton producing reaction rate was tallied and subtracted from the total reaction rate. Equivalently, each proton energy bin (Ebin) capture cross section is obtained using the following formula:

$$\Sigma_{c,Ebin}(x) = \frac{RR_{tot,Ebin}(x) - RR_{p\to p,Ebin}(x)}{\phi_{Ebin}(x)} \tag{4.9}$$

For alpha particles the capture cross section was neglected, because the outscattering cross section was orders of magnitude higher than the capture of alpha particles in the medium ($\Sigma_{c,\alpha} << \Sigma_{s,\alpha}$ so, $\Sigma_{c,\alpha} + \Sigma_{s,\alpha} \approx \Sigma_{s,\alpha}$). The resulting cross sections per energy bin are only space dependent, because MCNP6 has established these reaction rates using the energy distribution of the flux at each position (x). Therefore, these cross section are affected if one of the other cross section is changed. This effect is minimal for small changes. Hence, the energy distribution within each proton flux bin and the alpha flux, are assumed not to change after addition or adjustment of the cross sections.

To determine the outscattering cross sections needed for the model, first the outscatter cross section was determined for the highest proton energy bin. Since this energy bin equation has no source and no inscattering, the steady state total change for the highest energy bin protons is equal to negative the capture rate plus the outscatter rate. The steady state solution for the flux from MCNP6, was used to determine the total change $\frac{\partial\phi}{\partial x}$ between two slabs (x and x + dx). Using this value and the previously obtained capture cross section, the outscatter cross section could be determined by rewriting the steady state version of Equation 4.5 to:

$$\Sigma_{s,80}(x) = -\frac{\frac{\partial\phi_{p,80}}{\partial x} + \Sigma_{c,80}\phi_{p,80}}{\phi_{p,80}}. \tag{4.10}$$

To determine this outscatter for the next energy bin, the exact inscatter from the higher group was needed to solve an equation similar to Equation 4.10. Outscatter events that skips the energy group below is rare so

$$\Sigma_{s,80} = \Sigma_{s,80\to 7} + \Sigma_{s,80\to 2} + \Sigma_{s,80\to 0.5} \text{ with, } \Sigma_{s,80\to 7} >> \Sigma_{s,80\to 2} + \Sigma_{s,80\to 0.5}$$

$$\Sigma_{s,7} = \Sigma_{s,7\to 2} + \Sigma_{s,7\to 0.5} \text{ with, } \Sigma_{s,7\to 2} >> \Sigma_{s,7\to 0.5}.$$

Therefore, the approximation that $\Sigma_{s,80} = \Sigma_{s,80\to 7}$ and $\Sigma_{s,7} = \Sigma_{s,7\to 2}$ was used. Afterwards, Equation 4.11 and 4.12 were used to obtain the outscattering cross sections for the middle and lower energy bin respectively,

$$\Sigma_{s,7}(x) = -\frac{\frac{\partial \phi_{p,7}}{\partial x} + \Sigma_{c,7}\phi_{p,7} - \Sigma_{s,80}\phi_{p,80}}{\phi_{p,7}} \tag{4.11}$$

$$\Sigma_{s,2}(x) = -\frac{\frac{\partial \phi_{p,2}}{\partial x} + \Sigma_{c,2}\phi_{p,2} - \Sigma_{s,7}\phi_{7}}{\phi_{p,2}}. \tag{4.12}$$

For alpha particles no inscatter was used, but the flux change depended on the source at each location. For this reason the reaction rates were determined at each location for each energy bin. The reaction rates were determined specifically for each material, to separate the cross section for ^{11}B reactions from the ^{16}O reactions. The total change $\frac{\partial \phi}{\partial x}$ was again obtained from the same MCNP6 simulation and the capture cross section for alpha particles was assumed to be zero. To obtain the outscatter cross section, the steady state version of Equation 4.8 can be restructured to:

$$\Sigma_{s,\alpha}(x) = \frac{3[RR_{^{11}\mathrm{B},80,p\to\alpha} + RR_{^{11}\mathrm{B},7,p\to\alpha} + RR_{^{11}\mathrm{B},2,p\to\alpha}] + RR_{^{16}\mathrm{O},80,p\to\alpha} - \frac{\partial \phi_\alpha}{\partial x}}{\phi_\alpha} \tag{4.13}$$

$\Sigma_{B,Ebin}$ and Σ_O are the cross sections for alpha particles producing reactions and were obtained using the same method as for the capture cross section. The reaction rates used are established for reactions with ^{16}O and with ^{11}B separately for each energy bin. This is done to be able to change the cross section for the lowest energy protons. The boron reaction rates are multiplied by three, since three alpha particles per reaction are produced,

$$\Sigma_{B,Ebin} = 3 * \frac{RR_{^{11}\mathrm{B},p\to\alpha}}{\phi_{Ebin}},\ \Sigma_{H_2O,80} = \frac{RR_{H_2O,p\to\alpha}}{\phi_{p,80}}$$

Because the alpha flux data had a high variability, the resulting cross sections are smoothed by using an in-build function of Matlab called sgolayfilt. This is a data smoothing algorithm which takes each successive subset of 2m+1 data points and interpolates these points with a polynomial of order <2m [35]. This was done using a 4th order polynomial and 21 data points.

4.3 Non-dynamic model solver and accuracy verification

To verify the accuracy of the described model with the cross sections determined in Section 4.2.2, the steady state solution of the model was compared to the MCNP6 results. This non-dynamic model is a set of ordinary differential equations (ODE) (4.14-4.17) solved by a forward Euler method and by using ODE45, a Matlab ordinary differential equation solver. The set of ODE's used for simulation is:

$$\frac{\partial \phi_{p,80}(x)}{\partial x} = -[\Sigma_{s,80}(x) + \Sigma_{c,80}(x)]\phi_{p,80}(x) \tag{4.14}$$

$$\frac{\partial \phi_{p,7}(x)}{\partial x} = \Sigma_{s,80}(x)\phi_{p,80}(x) - [\Sigma_{s,7}(x) + \Sigma_{c,7}(x)]\phi_{p,7}(x) \tag{4.15}$$

$$\frac{\partial \phi_{p,2}(x)}{\partial x} = \Sigma_{s,7}(x)\phi_{p,7}(x) - [\Sigma_{s,2}(x) + \Sigma_{c,2}(x)]\phi_{p,2}(x) \tag{4.16}$$

$$\frac{\partial \phi_{\alpha}(x)}{\partial x} = [\Sigma_{B,80}(x) + \Sigma_O(x)]\phi_{p,80}(x) + \Sigma_{B,7}(x)\phi_{p,7}(x) + \Sigma_{B,2}(x)\phi_{p,2}(x) - \Sigma_{s,\alpha}(x)\phi_\alpha(x). \tag{4.17}$$

Figure 4.1 shows the variation and magnitude difference between cross sections. The variation in cross section is caused by the energy distribution changing, as the beam traverses through the medium. One example is the high variation in the outscatter cross section for the highest energy bin ($\Sigma_{s,80}$). This is the result of the average energy of the highest bin approaching the energy of the bin below. Consequently the chance of a scattering event resulting in energy loss high enough to move down one energy bin will increase. Therefore the cross section $\Sigma_{s,80}$ will increase drastically

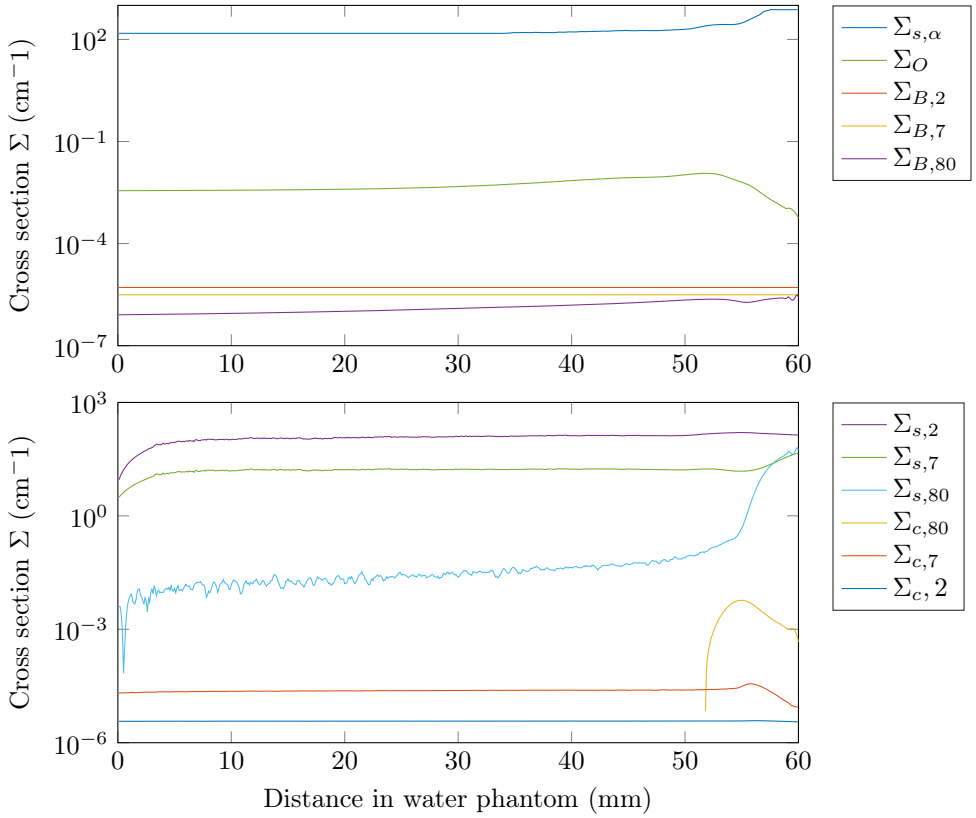

Figure 4.1: The cross sections obtained from the MCNP6 simulation, the top graph represents all cross sections used in Equation 4.17, to determine the alpha flux. The bottom graph shows the proton related scattering and capture cross sections for all energy bins. These cross sections are used in Equations 4.14 - 4.16.

with increasing distance in the phantom, as all protons will eventually leave this highest energy bin. The capture cross section for the highest energy bin ($\Sigma_{c,80}$) is negative for the first 50 mm of the geometry. Therefore, this cross section is only shown partly in the Figure 4.1. This negative $\Sigma_{c,80}$ is caused by multiple secondary proton generating reactions (^{16}O(p,xp)) in this first section of the geometry.

The system was 10 cm long and discretized in slabs of 1e-3 cm. The boundary condition is set to zero for all fluxes except for the highest energy bin protons for which $\phi_{p,80}(x = 0) = 0.01(\#/cm^2 s)$ is used. The latter value is the same as was obtained from MCNP6 for a simulation using a 10 x 10 x 10 cm phantom. Figure 4.2 depicting the resulting fluxes as well as their MCNP6 equivalent shows the non-dynamic model gives almost identical results as the MCNP6 data.

The ODE45 solver needed interpolation between cross section data, which was done using the interp1 Matlab function. This function uses linear interpolation between data points to find needed cross section points. The results for ODE45 and the forward Euler method are the same (see Appendix B).

The model was made to have easily adjustable cross sections, this is achieved by using all cross sections obtainable from one MCNP6 simulation. This simple model can solve the transport of protons and alpha particles, for the proton source energy and geometry used in the MCNP6 simulation. These variable can not be changed without a new simulation using MCNP6. The simple model matches MCNP6 well, this is the result of the cross section being calculated using the MCNP6 flux. This model can be used with changes to the cross sections. The co-dependence of cross sections is neglected in this model, which can cause the model the model accuracy to decrease. Therefore, the cross section modifications done should be only minor.

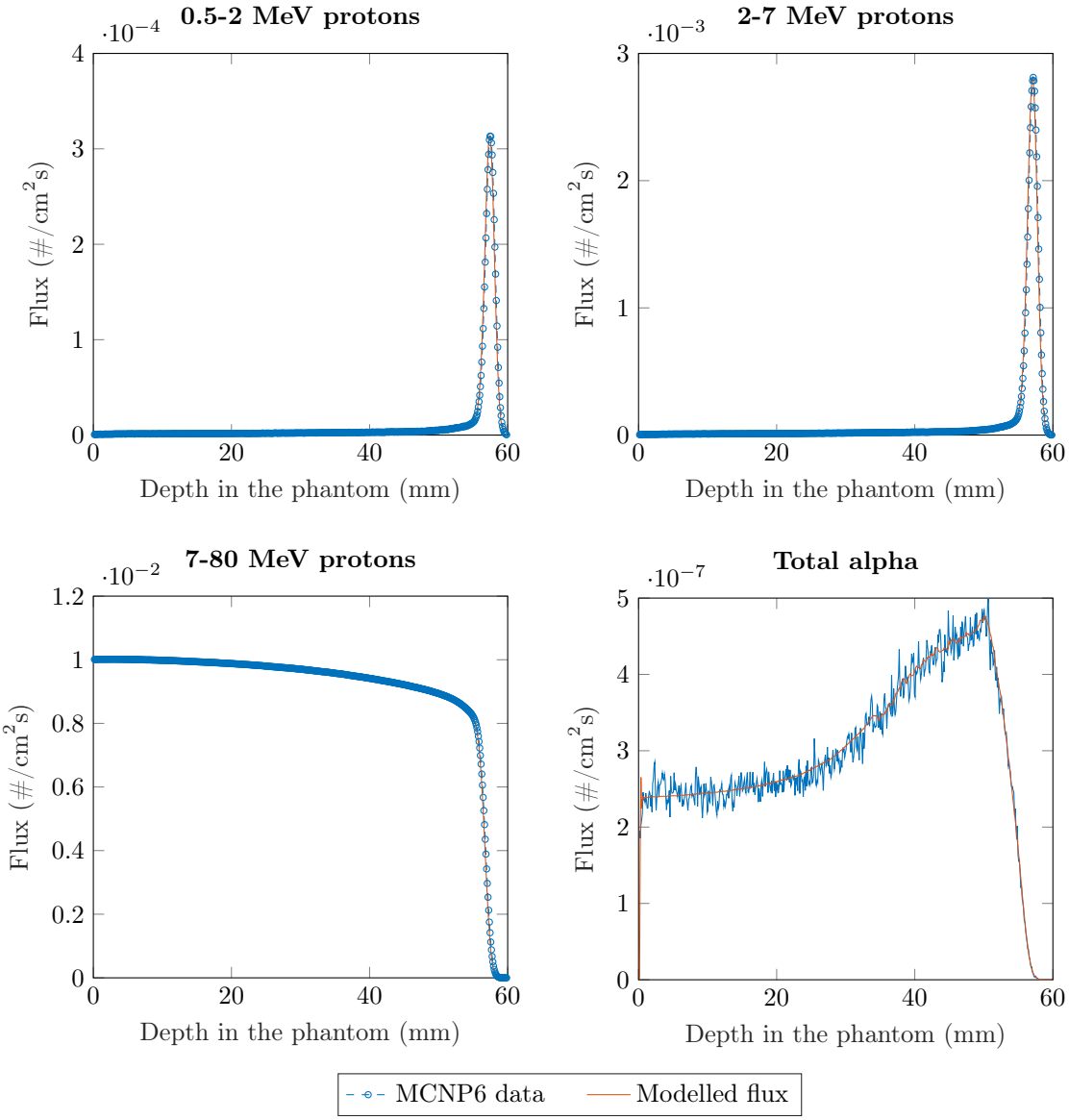

Figure 4.2: For each energy bin the MCNP6 tallied flux and the flux determined by solving the non-dynamic model. The lines overlap perfectly, except for the alpha flux. High variability in the results from MCNP6 is not obtained by the model, this is the result of applying a smoothing filter to the cross sections for alpha flux calculation.

4.4 Application of an alpha-proton-alpha avalanche reaction

The alpha-proton-alpha avalanche reaction was introduced by Eliezer et al. [33] to explain an unexpected increase in alpha production rate during boron fusion experiments. While the fusion conditions differ much from conditions that can be used during proton capture therapy, the avalanche mechanism might have an effect on the delivered dose, as result of high resting proton concentrations. The avalanche reaction is described in Figure 4.3. The reaction is initiated with an alpha particle hitting a resting proton, this proton will be accelerated to high enough energy (>0.5 MeV) to be captured by a ^{11}B. This capture reaction will cause the release of three alpha particles having enough energy to again accelerate a resting proton, causing a possible avalanche effect.

To investigate the effect of this avalanche reaction the cross section for alpha particles accelerating protons is needed. This cross section, within the energy range 1-8 MeV, is reported to be

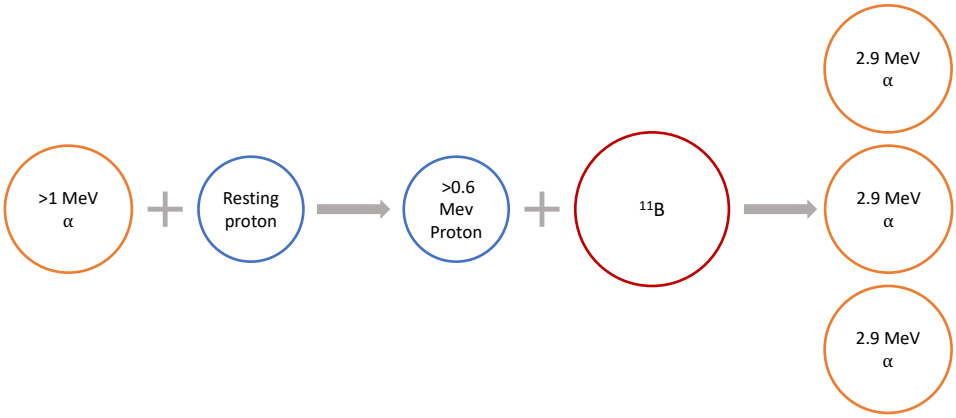

Figure 4.3: The alpha-proton-alpha avalanche reaction. An alpha particle hits a resting proton resulting in this proton being accelerated to high enough energy to react with a ^{11}B, to create three alpha particles. These three alpha particles could again create accelerated protons resulting in an avalanche of alpha particles created.

between 10 and 6 barns [36]. For further simulation, a fixed value of 8 barns is used for all positions, as this cross section has minimal energy dependence and therefore also no space dependence.

4.5 Description and discretization method for the dynamic model

Because the avalanche reaction is time dependent, the system of equations was not assumed to be steady state. The term $\Sigma_H \phi_\alpha$ was added as an alpha loss term to Equation 4.17, which is the macroscopic cross section of the alpha-proton acceleration multiplied by the alpha flux. Average alpha particle energy is approximately 2-3 MeV for alpha particles created from ^{11}B and can be up to 15 MeV for ^{16}O created alpha particles. Therefore, one alpha particle might accelerate multiple protons in one track. Hence $\Sigma_H \phi_\alpha$ is added to both Equation 4.15 and 4.16, for the middle and lowest energy bin protons respectively. This is assuming the alpha-proton hit rate is equally likely for both energies and for each alpha removed due to this reaction two protons are accelerated. The dynamic model is described by the following set of equations 4.18-4.21:

$$\frac{1}{v_{p,80}}\frac{\partial \phi_{p,80}(x,t)}{\partial t} + \frac{\partial \phi_{p,80}(x,t)}{\partial x} = -[\Sigma_{s,80}(x) + \Sigma_{c,80}(x)]\phi_{p,80}(x,t) \tag{4.18}$$

$$\frac{1}{v_{p,7}}\frac{\partial \phi_{p,7}(x,t)}{\partial t} + \frac{\partial \phi_{p,7}(x,t)}{\partial x} = \Sigma_H \phi_\alpha(x,t) + \Sigma_{s,80}(x)\phi_{p,80}(x,t) - [\Sigma_{s,7}(x) + \Sigma_{c,7}(x)]\phi_{p,7}(x,t) \tag{4.19}$$

$$\frac{1}{v_{p,2}}\frac{\partial \phi_{p,2}(x,t)}{\partial t} + \frac{\partial \phi_{p,2}(x,t)}{\partial x} = \Sigma_H \phi_\alpha(x,t) + \Sigma_{s,7}(x)\phi_{p,7}(x,t) - [\Sigma_{s,2}(x) + \Sigma_{c,2}(x)]\phi_{p,2}(x,t) \tag{4.20}$$

$$\frac{1}{v_\alpha}\frac{\partial \phi_\alpha(x,t)}{\partial t} + \frac{\partial \phi_\alpha(x,t)}{\partial x} = [\Sigma_{^{11}\mathrm{B},80}(x) + \Sigma_{H_2O}(x)]\phi_{p,80}(x,t) + \Sigma_{^{11}\mathrm{B},7}(x)\phi_{p,7}(x,t) + \Sigma_{^{11}\mathrm{B},2}(x)\phi_{p,2}(x,t) - [\Sigma_{s,\alpha}(x) + \Sigma_H]\phi_\alpha(x,t). \tag{4.21}$$

The velocity of the particles v is determined by the energy of the particle. Constant average velocity is assumed for the proton fluxes and the alpha flux. This average velocity is calculated using the simple formula with average energy for the each bin:

$$v_{particle,Ebin} = \sqrt{2\bar{E}m}$$

The discretization method used is similar to the method used in Section 4.3. The phantom is divided in slabs of 1e-3 cm, where for each slab the initial flux at t = 0 s, is determined by using the non-dynamic model with boundary condition $\phi_{p,80}$(x=0) = 1 proton/cm^{2}s. For the dynamic model the boundary condition is $\phi_{80}(x = 0, t > 0) = 0$, as the external proton source is no longer present. Solving the system of equations was done by applying a forward Euler method using time steps of 1e-13 seconds. For each slab, the $\frac{\partial \phi(x,t)}{\partial x}$ was determined by using the inflow $\phi(x - dx, t)$ and the outflow $\phi(x, t)$. 6000 time steps were used for simulation, or 600 picoseconds. The results of this simulation can be found in Figure 5.2 appearing in Section 5.2.

5 Parametric study of the dynamic and non-dynamic Boltzmann model

5.1 Effect of increased boron capture reactions below 1 MeV

The Monte Carlo methods used in Chapter 3 did not include the boron capture reactions below 1 MeV. This missing reaction will increase the alpha production rate. To explore the effect of this reaction on the energy deposited during proton boron capture therapy, the non-dynamic model was created. This model uses cross sections obtained from an MCNP6 simulation to determine the proton and alpha flux as function of depth in a water phantom. These cross sections can be adjusted to include proton capture below 1 MeV. The proton flux is split into three energy bins, the lowest bin ranges from 0.5 to 2 MeV, which is the relevant flux for below 1 MeV proton capture.

The reaction cross section for proton boron capture has peak value of 2.7 barn at 665 keV [17]. To add this cross section to the non-dynamic model, described in Section 4.3 by Equations 4.14 - 4.17, the alpha production cross section for the lowest energy protons $\Sigma_{B,2}$ is modified. This 2.7 barn is not valid for the complete energy bin, but only for the last fraction of this bin. However to overestimate any possible effect the average of the MCNP6 cross section and this 2.7 barn was used. The MCNP6 cross section was 1.3e-6 cm^{-1} and 2.7 barn converted to a macroscopic cross section was 9e-6 cm^{-1}, which resulted in a reaction cross section $\Sigma_{B,2}$ of 5.15e-6 cm^{-1}.

Using this updated cross section and the non-dynamic model the steady state fluxes were determined. The reaction rate for

$$p + {}^{11}\mathrm{B} \rightarrow 3\alpha,$$

was determined in each slab by multiplying the proton fluxes by their respective cross section for creating alpha particles. The alpha particle production increase can be seen in Figure 5.1. A small increase in reaction rate is shown at 57 mm, which is at the same location as the peak of the lowest energy proton flux. This is expected as the cross section for this flux is more than four times higher with this additional cross section. The proton flux in the lowest energy bin at x = 57 mm, is thirty times lower than the highest energy bin, hence resulting in only a small increase of approximately 5% in reaction rate at x = 57 mm.

To determine the total dose increase, the reaction rate had to be converted to energy deposition. This was achieved by multiplying the reaction rate in the Bragg peak volume, defined as x = 50 - 60 mm, with the average alpha particle energy of 5 MeV. To be able to compare this energy deposited to the 30 MeV proton energy deposited in the Bragg peak region (see Figure 1.4), a relative biological effectiveness (RBE) of 20 was used. The increased reaction rate had no significant effect on the total dose delivered in the Bragg peak volume. The dose increase was found to be 0.001% of the dose, delivered by the beam proton to this volume (3e-5 MeV).

5.2 Effects of a hypothesized alpha-proton-alpha avalanche reaction

To obtain the steady state dose increase from this avalanche reaction, the cross sections for the alpha proton acceleration are added to the non-dynamic model. This cross section is Σ_H, which is described in Section 4.4. The steady state dose increase due the addition of this avalanche reaction to the non-dynamic model is 4e-6 MeV (1e-4% of the total proton energy deposited). This value was expected to be low as the steady state alpha production rate from secondary protons $R_{p(\alpha)\rightarrow\alpha}$ is described by a combination of cross sections

$$R_{p(\alpha)\rightarrow\alpha} = \phi_\alpha * \Sigma_H * [\Sigma_{B,2} + \Sigma_{B,7}] \tag{5.1}$$

To explore the non-steady state effect of the avalanche reaction, the dynamic model described in Section 4.5 was used. The beam was stopped to explore a possible new steady state without

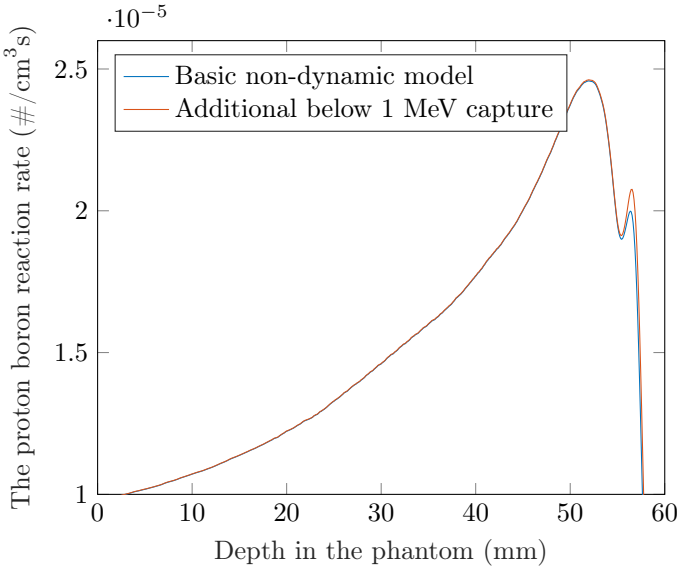

Figure 5.1: The reaction rate for the p + ^{11}B $\rightarrow 3\alpha$ reaction. The blue line was the basic non-dynamic model. The orange line is the result of adding the reaction below 1 MeV. A small increase in reaction rate can be seen at 57 mm.

source protons, therefore a simulation was performed over 6000 time steps of 1e-13 seconds each, at t = 0 the incoming proton beam is set to 0. The results depicted in Figure 5.2 show the four fluxes decreased fast over time for all positions in the phantom. Rather than reaching a new steady state, all fluxes decrease to zero after the 600 picosecond run, indicating the alpha-proton-alpha avalanche reaction is not a self sustaining chain reaction.

5.3 Parametric search for the experimentally found 50% increase in cell death

5.3.1 Analytic calculations

None of the simulations done replicated the effect found in the experimental work or simulations done. To obtain insight in the maximal achievable dose increase by proton boron capture, an analytic calculation was performed. The following formula was used to determine the reaction rate per incoming proton, and subsequently the dose increase per incoming proton:

$$\sigma_{^{11}B} * \rho_{n,^{11}B} = \#reactions/proton, \tag{5.2}$$

where $\sigma_{^{11}B}$ is the cross section for protons being captured by ^{11}B and creating three alpha particles. This cross section was multiplied with the number density of ^{11}B $\rho_{n,^{11}B}$. The only region of interest was the tumour area therefore the Bragg peak region. This region was defined to be the Bragg peak location $\pm$5 mm. For this region the reaction cross section $\sigma_{^{11}B}$, was assumed to be 1 barn through the whole Bragg peak. Each reaction results in the gain of 8.7 MeV, transferred to three alpha particles, this energy was assumed to be all deposited in the Bragg peak. Alpha particles have a higher relative biological effectiveness, the 8.7 MeV was multiplied by an RBE factor of 20 to obtain energy deposited per reaction.

To determine the number density of ^{11}B the concentrations used in the experimental work by Cirrone et al. [19] 100 ppm and simulation studies by Jung et al. [21] 1710 ppm were used. The analytically expected energy deposition increase, caused by the proton boron capture reaction, was determined for the concentrations reported in previous research. The expected increase was converted to a percentage by comparing the extra alpha energy to the proton energy deposition in the Bragg peak, which is approximately 30 MeV (see Figure 1.4). This expected increase in

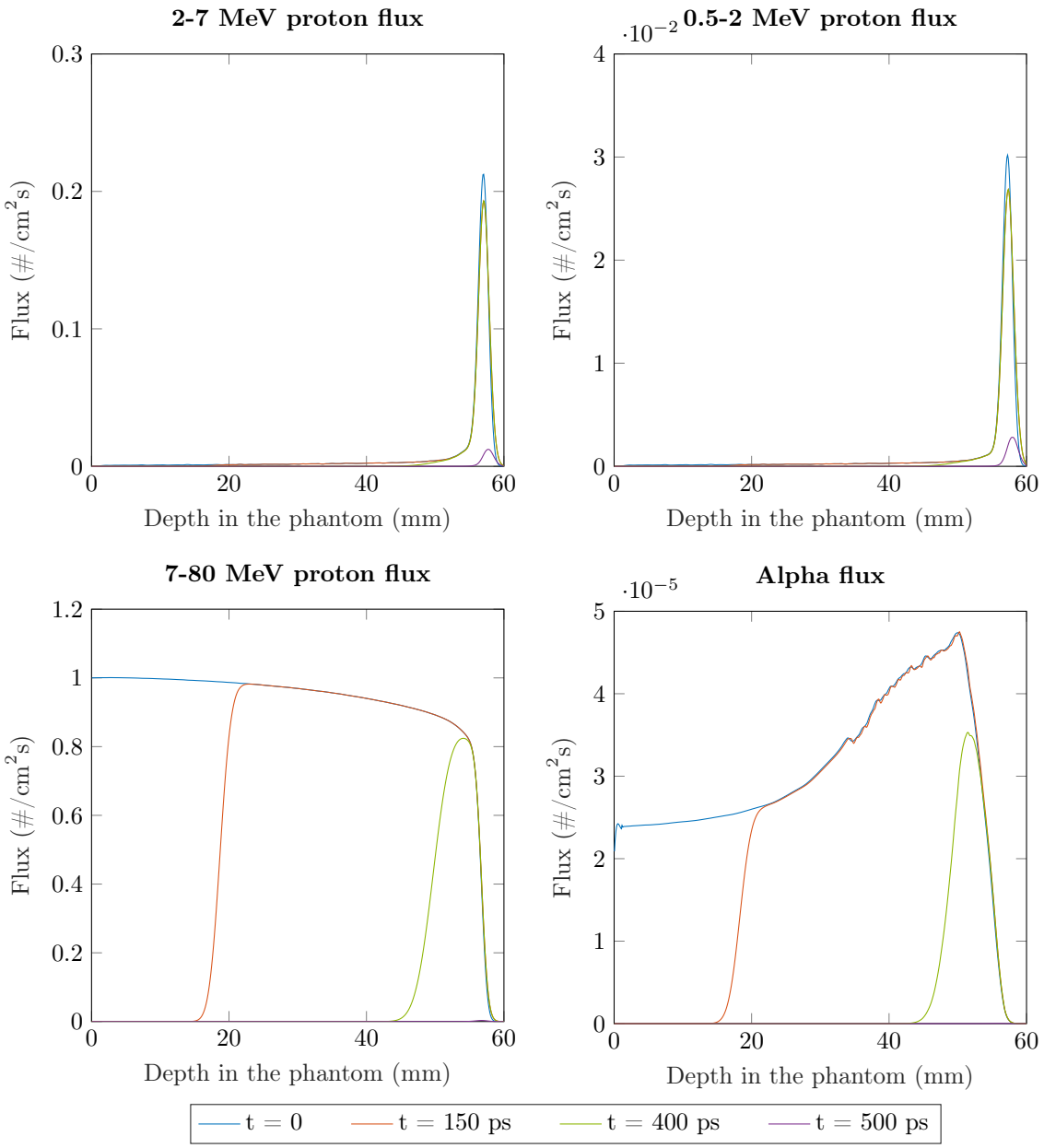

Figure 5.2: The flux for each energy and particle versus time. At t = 0 the incoming proton beam is stopped. The last plotted time point (500 ps) was chosen for proton flux 7-80 MeV is zero for the whole phantom. The alpha flux is zero and both lower energy bin proton fluxes are almost zero. These fluxes become zero less than 50 ps later so at the end of the 600 ps run all fluxes are zero throughout the phantom. This indicates the alpha-proton-alpha avalanche reaction is not self sustaining.

energy deposition was compared to increase reported in the two papers. The results are shown in Table 5.1, where the column "mismatch" refers to the ratio between reported and expected energy deposition increase. Note that the calculation were performed on the macro scale to determine the dose delivery. The experimentally found effects could be related to the reaction location and local alpha particle track creation. These latter effects will be discussed in the next section using a parametric search with the non-dynamic model. Using the concentration of 100 ppm the extra energy deposited was 8.7e-4, which deviates heavily from the 50% increase found during the experiments.

Table 5.1: Analytically calculated values for expected dose enhancement (%) compared to found values for two studies conducted.

Name	Concentration used (ppm)	Found (%)	Expected (%)	Mismatch
Jung et al. [21]	1710	90	5.00e-2	1.8e3
Cirrone et al. [19]	100	50*	2.91e-3	6.9e3

*The value found by Cirrone et al. was an increase in cell death instead of an actual dose increase.

5.3.2 Parameter variation needed for 50% increase in cell death

The results obtained by Jung et al. [21] could not be reproduced using simulation. The cell survival decrease reported by Cirrone et al. [19] was 50%, which can be due to the energy deposition increase. This increase was determined for the same concentration of ^{11}B used during the experiments. The energy deposition increase was determined using the five methods described in this thesis: MCNP6 (Section 3.1), Geant4(Section 3.2), analytic calculations (Section 5.3.1), non-dynamic model (Section 5.1) and with the addition of the avalanche reaction (Section 5.2). Figure 5.3 shows the resulting RBE corrected energy deposition increase for each of these methods. Compared to the 30 MeV of energy deposited per proton in the same region, each of the encountered increases is negligible. These results deviate substantially from the 50% increase in cell death reported by [19], which can be caused by the assumption that the ^{11}B is distributed uniformly true the cell. The microscopic distribution of boron, consequently the alpha production sites, may have a significant effect on the cell death resulting from alpha production.

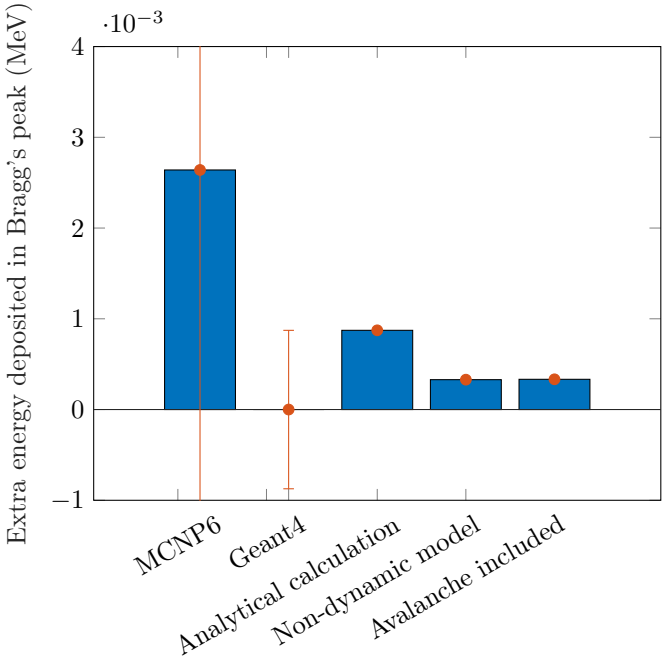

Figure 5.3: Summary of the simulated energy deposition increase for the geometry and concentration used by Cirrone et al. [19]. An alpha RBE of 20 is used for the values. The MCNP6 value is the highest. However the error for this value is three times the value. The error bars shown are purely statistical.

The distribution of the ^{11}B can be a significant contributor to the effective dose delivered by the produced alpha particles. To investigate this contribution, an optimal scenario is investigated for which the alpha particle production rate is determined. This rate can be converted to cells killed per alpha particle ratio using the data from the experiments done by Cironne et al. [19].

First, a production rate of alpha particles needed to be obtained from the non-dynamic model. The production rate from the ^{11}B in the Bragg peak was assumed to be at a peak value of 2.46e-5 alpha particles per proton (see Figure 5.1). The amount of protons in proton therapy is 6.2e8 protons/cm^3 for a 3 Gy fraction. Protons deposit 30 MeV of energy to the tumor area, this resulted in 1.53e4 alpha tracks per cm^3.

To describe the cell killing potential of these alpha tracks, the increase in cell death because of ^{11}B is obtained. Figure 5.4 depicting the experimental results by Cirrone et al. shows the increase is 15 percentage points. To translate this to cells killed, a cell density of 1e6 cell/cm^3 is used. For this case 1.5e5 cells are killed by 1.5e4 alpha tracks, implying ten cells are killed per alpha track. This applies to the most optimal case, when alpha particles only kill the cells not killed by the protons. Alpha particle track length, for a 5 MeV alpha particle, is approximately the size of one cell.

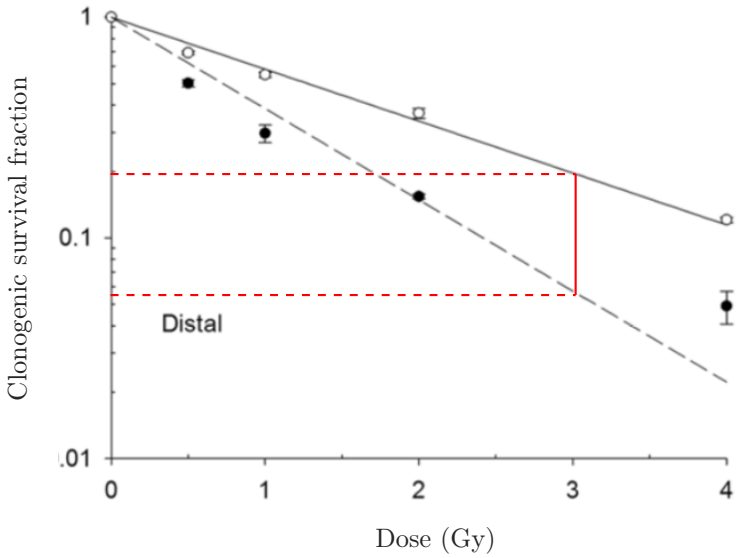

Figure 5.4: Result obtained by Cirrone et al. [19]. The increase in cell death at 3 Gy is approximately 15 percentage points.

5.4 Discussion

The difference between MCNP6 and Geant4 shown in Figure 5.3 can be contributed to the cross section difference between the two codes. MCNP6 was used with the TENDL2017 cross sections, including a proton capture cross section for ^{11}B. Geant4 did not have this proton capture cross section, which may lead to a lower difference between the boron and non boron run.

The results obtained from the dynamic model provide just an indication of the expected dose increase. Note that this model is rather basic and many assumptions had to be made, though most assumptions were in favor of achieving an increase in energy deposited due to the proton-boron-alpha reaction. The one-directional streaming assumption drives the particles out of the phantom. For more accurate results, particles should be tracked individually, which could be implemented using time-dependent Monte Carlo methods.

6 Conclusion

To determine the feasibility of proton boron capture therapy, several simulation routes were explored. As a first step, MCNP6 was used to determine whether an increase in energy deposition arises when implementing a boron uptake region in the Bragg peak area. These initial simulations showed no increase in energy deposited, a result diverging very much from previously found results [21]. To check whether these results were specific for MCNP6, the same geometry and settings were used together with Geant4, which however again resulted in no effective dose increase. Thus, neither MCNP6 or Geant4 presented any relevant dose increase due to proton boron capture for reasonable boron concentrations ($<$ 1000ppm).

MCNP6 and Geant4 simulations were based on cross section libraries which did not include all possible alpha generating reactions. The two missing reactions of interest were below 1 MeV proton boron capture and the avalanche reaction. Therefore, using a simple Boltzmann model based on MCNP6 cross sections the effects of these two reactions were investigated. Also for these two reactions no significant contribution to the total dose delivered was found. However, below 1 MeV proton capture turned out to increase ^{11}B alpha production by approximately 5 % at the distal end of the Bragg peak.

Using the most optimistic cross sections and alpha removal settings in the simple Boltzmann model, an alpha production rate was determined. From the experiments done, the total cell killing potential of these created alpha particles was used to determine the cells killed per alpha particle. This number turned out to be unrealistic, even though this was done using optimistic parameters.

In conclusion, the proton boron capture reaction is not expected to be functional for enhancement of proton therapy efficiency based on the performed simulations. The cross section, and correspondingly the reaction chance, are too low for a significant effect. A possible explanation for the experimental results is the increase of general radio sensitivity of the cell, caused by boron being present in the cell. Further research is needed to investigate this, for instance, with an experiment irradiating boronated and unboronated cell cultures with gamma ray.

Bibliography

[1] M. Valdivieso, A. M. Kujawa, T. Jones, and L. H. Baker, "Cancer survivors in the united states: a review of the literature and a call to action," *International journal of medical sciences*, vol. 9, no. 2, p. 163, 2012.

[2] G. Delaney, S. Jacob, C. Featherstone, and M. Barton, "The role of radiotherapy in cancer treatment: estimating optimal utilization from a review of evidence-based clinical guidelines," *Cancer: Interdisciplinary International Journal of the American Cancer Society*, vol. 104, no. 6, pp. 1129–1137, 2005.

[3] J. R. Carver, C. L. Shapiro, A. Ng, L. Jacobs, C. Schwartz, K. S. Virgo, K. L. Hagerty, M. R. Somerfield, and D. J. Vaughn, "American society of clinical oncology clinical evidence review on the ongoing care of adult cancer survivors: Cardiac and pulmonary late effects," *Journal of Clinical Oncology*, vol. 25, no. 25, pp. 3991–4008, 2007. PMID: 17577017.

[4] R. R. Wilson, "Radiological use of fast protons," *Radiology*, vol. 47, no. 5, pp. 487–491, 1946.

[5] P. Blanchard, A. S. Garden, G. B. Gunn, D. I. Rosenthal, W. H. Morrison, M. Hernandez, J. Crutison, J. J. Lee, R. Ye, C. D. Fuller, A. S. Mohamed, K. A. Hutcheson, E. B. Holliday, N. G. Thaker, E. M. Sturgis, M. S. Kies, X. R. Zhu, R. Mohan, and S. J. Frank, "Intensity-modulated proton beam therapy (impt) versus intensity-modulated photon therapy (imrt) for patients with oropharynx cancer – a case matched analysis," *Radiotherapy and Oncology*, vol. 120, no. 1, pp. 48 – 55, 2016.

[6] P. Blanchard, G. B. Gunn, A. Lin, R. L. Foote, N. Y. Lee, and S. J. Frank, "Proton therapy for head and neck cancers," *Seminars in Radiation Oncology*, vol. 28, no. 1, pp. 53 – 63, 2018. Head and Neck Cancer Update.

[7] D. C. Weber, H. Wang, L. Cozzi, G. Dipasquale, H. G. Khan, O. Ratib, M. Rouzaud, H. Vees, H. Zaidi, and R. Miralbell, "Rapidarc, intensity modulated photon and proton techniques for recurrent prostate cancer in previously irradiated patients: a treatment planning comparison study," *Radiation Oncology*, vol. 4, no. 1, p. 34, 2009.

[8] J. M. Verburg, *reducing range uncertainty in proton therapy*. PhD thesis, Eindhoven University of Technoly, 2015.

[9] T. Mitin and A. L. Zietman, "Promise and pitfalls of heavy-particle therapy," *Journal of Clinical Oncology*, vol. 32, no. 26, p. 2855, 2014.

[10] Bozkurt, Ahmet, "Monte carlo calculation of proton stopping power and ranges in water for therapeutic energies," *EPJ Web Conf.*, vol. 154, p. 01007, 2017.

[11] B. Gottschalk, A. Koehler, R. Schneider, J. Sisterson, and M. Wagner, "Multiple coulomb scattering of 160 mev protons," *Nuclear Instruments and Methods in Physics Research Section B: Beam Interactions with Materials and Atoms*, vol. 74, no. 4, pp. 467–490, 1993.

[12] S. B. Jia, M. H. Hadizadeh, A. A. Mowlavi, and M. E. Loushab, "Evaluation of energy deposition and secondary particle production in proton therapy of brain using a slab head phantom," *Reports of Practical Oncology & Radiotherapy*, vol. 19, no. 6, pp. 376–384, 2014.

[13] R. F. Barth, J. A. Coderre, M. G. H. Vicente, and T. E. Blue, "Boron neutron capture therapy of cancer: current status and future prospects," *Clinical Cancer Research*, vol. 11, no. 11, pp. 3987–4002, 2005.

[14] R. L. Moss, "Critical review, with an optimistic outlook, on boron neutron capture therapy (bnct)," *Applied Radiation and Isotopes*, vol. 88, pp. 2–11, 2014.

[15] H. Koivunoro, L. Kankaanranta, and H. Joensuu, "A dose response analysis of head and neck cancer patients treated with boron neutron capture therapy (bnct)," *International Journal of Radiation Oncology*, vol. 96, no. 2, p. E387, 2016.

[16] R. F. Barth, M. H. Vicente, O. K. Harling, W. Kiger, K. J. Riley, P. J. Binns, F. M. Wagner, M. Suzuki, T. Aihara, I. Kato, *et al.*, "Current status of boron neutron capture therapy of high grade gliomas and recurrent head and neck cancer," *Radiation Oncology*, vol. 7, no. 1, p. 146, 2012.

[17] J. Liu, X. Lu, X. Wang, and W.-K. Chu, "Cross-sections of 11b(p,α)8be reaction for boron analysis," *Nuclear insturments and Methods in Physics Research*, vol. 96, pp. 107–111, 2002.

[18] D.-K. Yoon, J.-Y. Jung, and T. S. Suh, "Application of proton boron fusion reaction to radiation therapy: A monte carlo simulation study," *Applied Physics Letters*, vol. 105, no. 22, p. 223507, 2014.

[19] G. Cirrone, L. Manti, D. Margarone, G. Petringa, L. Giuffrida, A. Minopoli, A. Picciotto, G. Russo, F. Cammarata, P. Pisciotta, *et al.*, "First experimental proof of proton boron capture therapy (pbct) to enhance protontherapy effectiveness," *Scientific reports*, vol. 8, no. 1, p. 1141, 2018.

[20] A. Mazzone, P. Finocchiaro, S. L. Meo, and N. Colonna, "On the (un) effectiveness of proton boron capture in proton therapy," *arXiv preprint arXiv:1802.09482*, 2018.

[21] J.-Y. Jung, D.-K. Yoon, B. Barraclough, H. C. Lee, T. S. Suh, and B. Lu, "Comparison between proton boron fusion therapy (pbft) and boron neutron capture therapy (bnct): a monte carlo study," *Oncotarget*, vol. 8, no. 24, p. 39774, 2017.

[22] J.-Y. Jung, D.-K. Yoon, H. C. Lee, B. Lu, and T. S. Suh, "The investigation of physical conditions of boron uptake region in proton boron fusion therapy (pbft)," *AIP Advances*, vol. 6, no. 9, p. 095119, 2016.

[23] E. M. Hussein, "Chapter four - transport," in *Radiation Mechanics* (E. M. Hussein, ed.), pp. 247 – 310, Oxford: Elsevier Science Ltd, 2007.

[24] W. L. Dunn and J. K. Shultis, "10 - monte carlo simulation of neutral particle transport," in *Exploring Monte Carlo Methods* (W. L. Dunn and J. K. Shultis, eds.), pp. 269 – 306, Amsterdam: Elsevier, 2012.

[25] C. J. Werner, *MCNP user's manual - Code Version 6.2.* Los Alamos Nuclear Laboratory, New Mexico, 10 2017.

[26] M. Herman and A. Trkov, *ENDF-6 Formats Manual.* National Nuclear Data Center, Brookhaven National Laboratory, Upton, 7 2010.

[27] S. Agostinelli *et al.*, "Geant4 — a simulation toolkit," *Nuclear Instruments and Methods in Physics Research Section A: Accelerators, Spectrometers, Detectors and Associated Equipment*, vol. 506, no. 3, pp. 250 – 303, 2003.

[28] H. Fuchs, S. Vatnitsky, M. Stock, D. Georg, and L. Grevillot, "Evaluation of gate/geant4 multiple coulomb scattering algorithms for a 160mev proton beam," *Nuclear Instruments and Methods in Physics Research Section B: Beam Interactions with Materials and Atoms*, vol. 410, pp. 122 – 126, 2017.

[29] "`https://geant4.web.cern.ch/`," Aug 2018.

[30] D. Rochman, A. Koning, J. C. Sublet, M. Fleming, E. Bauge, S. Hilaire, P. Romain, B. Morillon, H. Duarte, S. Goriely, *et al.*, "The tendl library: Hope, reality and future," in *EPJ Web of Conferences*, vol. 146, p. 02006, EDP Sciences, 2017.

[31] R. F. Barth, A. H. Soloway, and R. G. Fairchild, "Boron neutron capture therapy for cancer," *Scientific American*, vol. 263, no. 4, pp. 100–107, 1990.

[32] A.Bagulya, I.Gudowska, V.Ivanchenko, and N.Starkov, "`http://geant4-userdoc.web.cern.ch/geant4-userdoc/Doxygen/examples_doc/html/ExampleHadr01.html`," Aug 2018.

[33] S. Eliezer, H. Hora, G. Korn, N. Nissim, and J. M. Martinez Val, "Avalanche proton-boron fusion based on elastic nuclear collisions," *Physics of Plasmas*, vol. 23, no. 5, p. 050704, 2016.

[34] Y. Oka and T. Kiguchi, "Nuclear reactor design (an advanced course in nuclear engineering)," 2014.

[35] A. Savitzky and M. J. Golay, "Smoothing and differentiation of data by simplified least squares procedures.," *Analytical chemistry*, vol. 36, no. 8, pp. 1627–1639, 1964.

[36] J. Keay and D. Ingram, "Absolute cross section for forward recoiling hydrogen with 1.0–12.5 mev 4he," *Nuclear Instruments and Methods in Physics Research Section B: Beam Interactions with Materials and Atoms*, vol. 211, no. 3, pp. 305–311, 2003.

A Appendix: MCNP6 input file used to reproduce results by Jung al.

```
F6hF16a80MeVmat10B6-5       $ file name
c ---- Cell Card --------
1 0 1 .. 100    IMP:H,A=0   $ void created
1001 1.0 -1 -1  IMP:H,A=1   $ start of water cells
                            $ cell 1002-10050 removed
1051 1.0 -1 -51 IMP:H,A=1   $ cell removed are same material
1052 3 -1 -52   IMP:H,A=1   $ start of the BUR
                            $ cell 1053-1060 removed
1061 3 -1 -61 IMP:H,A=1     $ end of the BUR
1062 1.0 -1 -62 IMP:H,A=1   $ behind BUR water
                            $ cell 1063-1099 removed
1100 1.0 -1 -100 IMP:H,A=1  $ end of geometry
c------------------------

c ---- Surface Cards ----
1 rpp 0.0 0.1 -5.0 5.0 -5.0 5.0     $ first slab of the geometry
                                    $ surface cards 2-99 removed
100 rpp 9.9 10.0 -5.0 5.0 -5.0 5.0  $ last slab of the geometry
c ------------------------

c ---- Data Cards -------
c ---- Tally Card -------
F6:h      1001 .. 1100              $ the F6 energy deposition tally for protons
F16:a      1001 .. 1100             $ the F6 tally for alpha particles
c ---- Material card ----
 M1 1002.17h 2 8016.17h 1           $ water material
 M2 5011.17h -1 $ boron11           $ pure boron11
 M3 1002.17h 0.66667 8016.17h 0.33333 5011.17h 0.0001   $ material for BUR
c ---- Cutoff energy ----
 CUT:H J 1e-1                       $ proton cut off
 CUT:A,D,T,S  J  1e-3               $ other particle cut off
c ---- Physics card -----
 PHYS:H 200 0 -1 J 0 J 0 J J J 0 0 0 0.917 0 0
 MODE H a n d p e t s #$ Mode has to be all
c ---- Source definition -
 NPS 2000000                        $ amount of histories to create
 SDEF X=0.000001 Y=0 Z=0 PAR=h ERG=80 VEC=1 0 0 DIR=1   $ source
```

B Appendix: ODE45 compared to non-dynamic model

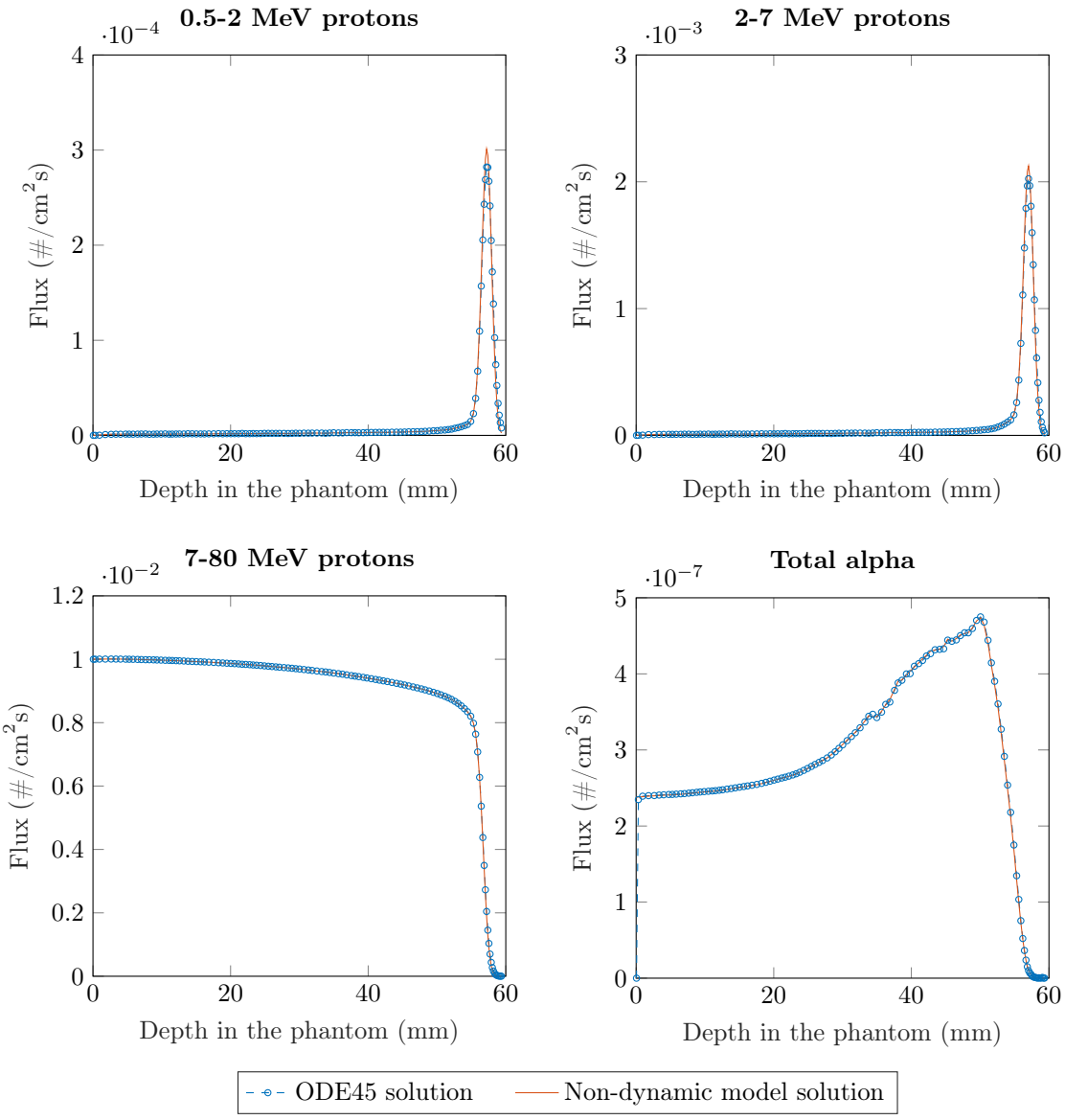

Figure B.1: The fluxes obtained via solving Equations 4.8 - 4.14, through the forward Euler method compared to using the build in Matlab function ODE45. The same cross sections and equations were used for both methods.

C Appendix: Matlab code for the non-dynamic model

```
function [FiltFlux, alphaProdB11] = nonDynMod(c, lowMeV, conBoron)
% c is the multiplier for the proton production from the avalanche, low
% low MeV is the below one MeV reaction cross-section multiplier
% conBoron is the concentration of boron
Backend=xlsread('~/Documents/Thesis/Workingfiles/WorkingFilesOctober.xlsx'...
                ,'BackendDynModV3');

SigmaH_tot = 4.14e-1;
pMatrix = Backend(3:17,67:70);
Source = 1; %starting proton count
dx = 0.01; %cm

SigmaB_2 = pMatrix(2,1);

% boundary conditions applied
FluxH = zeros(3,608);
FluxH(:,1,1) = [2;7;80];
FluxH0 = [0;0;Source];
FluxA = zeros(1,608);
FluxA(1:2) = [0,2.37e-7];
dFluxX = [0;0;0];
AlphaProduction = [0,0];

FluxH(:,2) = FluxH0;

mesh = 0.05:0.1:60.6; %create geometry used.

load('SigmaPDE.mat') %Load all cross-sections
CrossSections = SigmaPDE.';

%sweeping from left to right using forward euler
for i = 2:600
    % Determine for the next step the dflux/dx for proton fluxes
    dFluxX(1) = ((-CrossSections(4,i-1)-CrossSections(1,i-1))*FluxH(1,i)...
                +CrossSections(5,i-1)*FluxH(2,i)+c*SigmaH_tot*FluxA(i))*dx;
    dFluxX(2) = ((-CrossSections(5,i-1)-CrossSections(2,i-1))*FluxH(2,i)...
                +CrossSections(6,i-1)*FluxH(3,i)+c*SigmaH_tot*FluxA(i))*dx;
    dFluxX(3) = ((-CrossSections(6,i-1)-CrossSections(3,i-1))*FluxH(3,i))...
                *dx;

    %determine dflux/dx for alpha particles
    dFluxAlpha(i) = (AlphaProduction(i) - CrossSections(12,i)*FluxA(i)...
                    -SigmaH_tot*FluxA(i))*dx;

            %update the three proton fluxes
            for j = 1:3
                FluxH(j,i+1) = FluxH(j,i) + dFluxX(j);
            end
     %Determine intermediate alpha production for each locations
     AlphaProduction(i) = conBoron*3*(lowMeV*SigmaB_2*FluxH(1,i) ...
       + CrossSections(10,i)*FluxH(2,i) + CrossSections(11,i)*FluxH(3,i))...
```

```
      + CrossSections(13,i)*FluxH(3,i);
     alphaProdB11(i) = conBoron*3*(lowMeV*SigmaB_2*FluxH(1,i)...
      + CrossSections(10,i)*FluxH(2,i) + CrossSections(11,i)*FluxH(3,i));

    % make substep routine for alpha flux tail if trying to overshoot
        if dFluxAlpha(i) > 20*dFluxAlpha(i-1)
            substeps = 100;
            dx = dx/substeps;
            subFlux(1) = FluxA(i);

            for k = 1:substeps
                dsub(k) = (AlphaProduction(i) - CrossSections(12,i)...
                            *subFlux(k)-SigmaH_tot*subFlux(k))*dx;
                subFlux(k+1) = subFlux(k) + dsub(k);
            end

            FluxA(i+1) = subFlux(substeps);
            dx = dx*substeps;
        else

        %update alpha flux for next step
            FluxA(i+1) = FluxA(i) + dFluxAlpha(i);
        end


end

FiltFlux(1,:) = sgolayfilt(FluxH(1,3:end), 4, 21);
FiltFlux(2,:) = sgolayfilt(FluxH(2,3:end), 4, 21);
FiltFlux(3,:) = sgolayfilt(FluxH(3,3:end), 4, 21);
FiltFlux(4,:) = sgolayfilt(FluxA(3:end), 4, 21);
```

D Appendix: Matlab code for the dynamic model

```
%determine particle speed
c = 3e10; %cm/s
v_2 = sqrt(2*2/931.5)*c;
v_7 = sqrt(7*2/931.5)*c;
v_80 = sqrt(80*2/931.5)*c;
v_alpha = sqrt(5*2/(931.5*4))*c;

timesteps = 6000;
newX = 0.05:0.1:60;
dt = 1e-13;                 %chose a dt in seconds
dx = (newX(2)-newX(1))*0.1; %dx needs to be in cm

FluxT = zeros(4,length(newX),timesteps);
Sigma = SigmaPDE.';         %cross-sections

%initial condition is obtained from non-dynamic model FiltFlux
for i = 1:4
FluxT(i,:,1) = interp1(mesh,FiltFlux(i,:),newX);
end

% interate over all timesteps
for t = 1:timesteps
    %determine Q = all sources of particles withouth streaming
    for i = 2:(length(newX)-1)

       Q_2(i,t) = Sigma(5,i) * FluxT(2,i,t) + SigmaH_2 ...
       * FluxT(4,i,t) - (Sigma(4,i) + Sigma(1,i))*FluxT(1,i,t) ;
       Q_7(i,t) = Sigma(6,i) * FluxT(3,i,t) + SigmaH_7 ...
       * FluxT(4,i,t) - (Sigma(5,i) + Sigma(2,i))*FluxT(2,i,t) ;
       Q_80(i,t) =   - (Sigma(6,i) + Sigma(3,i))*FluxT(3,i,t) ;

       stop_alpha(i,t) =  - Sigma(12,i)*FluxT(4,i,t) ...
       - SigmaH_tot*FluxT(4,i,t);

       Q_alpha(i,t) = 4*3*(SigmaB_2*FluxT(1,i,t) + Sigma(10,i)...
       *FluxT(2,i,t) + Sigma(11,i)*FluxT(3,i,t)) ...
       + Sigma(13,i)*FluxT(3,i,t);

       %in minus out streaming
       dFdx_2(i,t) =        (FluxT(1,i-1,t) - FluxT(1,i,t))/(dx);
       dFdx_7(i,t) =        (FluxT(2,i-1,t) - FluxT(2,i,t))/(dx);
       dFdx_80(i,t) =       (FluxT(3,i-1,t) - FluxT(3,i,t))/(dx);
       dFdx_alpha(i,t) =    (FluxT(4,i-1,t) - FluxT(4,i,t))/(dx);

       %total change over time
       dFluxT(1,i,t) = (Q_2(i,t)    +   dFdx_2(i,t))            *v_2*dt;%
       dFluxT(2,i,t) = (Q_7(i,t)    +   dFdx_7(i,t))            *v_7*dt;%
       dFluxT(3,i,t) = (Q_80(i,t)   +   dFdx_80(i,t))           *v_80*dt;
       dFluxT(4,i,t) = (Q_alpha(i,t) + dFdx_alpha(i,t) ...
        + stop_alpha(i,t))*v_alpha*dt; %
```

```
        %update flux for the next time step
        for j = 1:4
                FluxT(j,i,t+1) = FluxT(j,i,t) + dFluxT(j,i,t);
        end
    end
end
```